Electrochemical, postmortem, and safety evaluation of practical high-voltage (NMC-811) Li metal batteries with hybrid ceramic polymer electrolyte

Nicola Boaretto, Haritz Perez-Furundarena, Leire Meabe, Simon Lindberg, Izaskun Combarro, Andriy Kvasha, Ekin Esen, Diego del Olmo, Elixabete Ayerbe, Hendrix Demers, et al.

Electrochemical, Postmortem, and Safety Evaluation of Practical High-Voltage (NMC-811) Li Metal Batteries with Hybrid Ceramic Polymer Electrolyte

Nicola Boaretto,[1,*] Haritz Perez-Furundarena,[1] Leire Meabe,[1] Simon Lindberg,[1] Izaskun Combarro,[2] Andriy Kvasha,[2] Ekin Esen,[2] Diego del Olmo,[2] Elixabete Ayerbe,[2] Hendrix Demers,[3] Abdelbast Guerfi,[3] Rémi Vincent,[4] Jérôme Cognard,[4] Sylvie Genies,[4] Marine Lechartier,[4] Lise Daniel,[4] Adrien Mery,[5] Laurent Castro,[6] Aurelie Gueguen,[6] María Martinez-Ibañez.[1]

[1] *Centre for Cooperative Research on Alternative Energies, CIC energiGUNE, Basque Research and Technology Alliance (BRTA), Alava Technology Park, Albert Einstein 48, Vitoria-Gasteiz 01510, Spain*

[2] *CIDETEC, Basque Research and Technology Alliance (BRTA), Paseo de Miramon 196, Donostia-San Sebastian 20014, Spain*

[3] *Center of Excellence in Transportation Electrification and Energy Storage (CETEES), Hydro-Québec, 1806 Boul. Lionel-Boulet, Varennes, Québec J3X 1S1, Canada*

[4] Univ. Grenoble Alpes, CEA, Liten, F-38000 Grenoble, France

[5] *AMPERE, AMV-CPB5, Batterie Chimie Recherche, Technocentre Renault, 1 avenue du golf, 78084, Guyancourt, France*

[6] *Toyota Motor Europe, Hoge Wei 33 B, B-1930 Zaventem, Belgium*

[*] *nboaretto@cicenergigune.com*

Keywords: *Li metal solid-state batteries, polymer electrolytes, high voltage, multilayer pouch cells, thermal runaway, safety*

Highlights:

- Double-coated HCPE improves interface and cycling in Li||Li cells.
- 1 Ah pouch cells retain ~90% capacity after 90 cycles at high loading.
- Lithium corrosion causes rapid failure after 90 cycles in pouch cells.
- Safety is similar to commercial LIBs; thermal runaway energy higher due to Li.

Abstract

In this work, cycling and safety performance of high-voltage lithium polymer batteries, in multilayer pouch cell configuration, are studied. The batteries encompass a hybrid ceramic polymer electrolyte, high loading cathode based on $LiNi_{0.8}Mn_{0.1}Co_{0.1}O_2$ (NMC-811), and 40 μm-thick self-standing Li metal anodes. Solid state NMC-811-based cathodes for the multilayer pouch cells were produced with practical areal capacities of 2.7 $mAh \cdot cm^{-2}$. Pouch cells with nominal capacity of 1 Ah reached specific energy of 358 $Wh \cdot kg^{-1}$. Cells cycled at 60 °C and C/10 showed 85% capacity retention at the 90^{th} cycle, followed by rapid failure before the 100^{th} cycle. Postmortem analysis indicated that rapid failure is caused by lithium anode exhaustion, exacerbated by the large areal capacity, in accordance with observations in Li||Li symmetric cells. Finally, overtemperature tests in closed calorimeter were performed on 1 Ah and 3 Ah pouch Li/NMC811 cells. The cells showed similar safety behavior to commercial lithium-ion batteries. The released energy was higher, which is attributed to the contribution of the lithium metal as the anode. This study demonstrates the possibilities and challenges of high-voltage lithium metal batteries with polyether-based electrolytes, in terms of performance and safety, in a realistic cell configuration.

Introduction

Lithium-ion batteries (LIBs) are the main electrochemical energy storage devices for powering portable electronics and battery electric vehicles (BEV), and their use is set to increase owing

to the need of reducing the consumption of fossil fuels. In 2030, the global LIBs demand is estimated to reach around 4.7 TWh [1]. In particular, the electrification of the automotive sector will be the main driver for the increase in battery demand, owing to the urgent need to reduce the consumption of fossil fuels. Still, the mass market penetration of BEV is hindered by several factors, such as their high cost, charging speed, and limited driving range [2,3]. Besides increasing the size of the battery pack, which is feasible for larger vehicles, another way to increase the driving range is to increase the energy density at pack or cell level. Most of LIBs currently reach values of 260 $Wh \cdot kg^{-1}$ and 700 $Wh \cdot L^{-1}$ at cell level [4]. For comparison, the US Department of Energy targets for non-fast-charge batteries for BEVs, at cell level, are 350 $Wh \cdot kg^{-1}$ and 750 $Wh \cdot L^{-1}$, respectively [5]. Higher energy contents may be achieved by combining high energy active materials, such as Ni-rich layered oxides at the positive electrode, and metallic lithium at the negative one [6]. Cells with this configuration may reach specific energy over 400 $Wh \cdot kg^{-1}$, thanks to the high specific capacity (3860 $mAh \cdot g^{-1}$) and low electrode potential (−3.04 V *vs.* standard hydrogen electrode) of metallic lithium [7]. The use of lithium metal anodes, however, is problematic owing to its high reactivity and to the risk of short circuits, with the associated safety concerns, especially in combination with highly flammable carbonate-based liquid electrolytes [8]. Thus, the use of lithium metal must be accompanied by a shift towards safer, non-flammable electrolytes, such as solid-state electrolytes [9–11]. These can be roughly divided between inorganic solid-state electrolytes and polymer electrolytes. Both classes present advantages and drawbacks, with the inorganic electrolytes having higher ionic conductivities, and polymer electrolytes having better processability and more advantageous mechanical properties [12].

One of the issues with polymer electrolytes regards their limited oxidative stability. It is generally accepted that poly(ethylene oxide) and other polyethers oxidize at potentials of around 4 V *vs.* Li/Li^+ at 60-80ºC [13], although some recent studies have proposed kinetic

stabilization up 4.5 V *vs.* Li/Li^+ [14]. Furthermore, some particularly reactive cathode chemistries, such as the layered oxides of transition metals (Co, Mn, and Ni), can facilitate polymer electrolyte degradation [15,16]. For these reasons, the use of polymer electrolytes has been traditionally restricted to low-voltage lithium-metal batteries, that is, in combination with 3 V-class cathode active materials (CAM) such as $LiFePO_4$. Only in recent years, driven by the need of increasing the cell energy density, polymer electrolytes have been increasingly tested with high-voltage CAM, especially with $LiCoO_2$, Ni-rich layered oxides like $LiNi_{0.6}Mn_{0.2}Co_{0.2}O_2$ (NMC-622) and $LiNi_{0.8}Mn_{0.1}Co_{0.1}O_2$ (NMC-811), and $LiFe_xMn_{(1-x)}PO_4$ [17–19]. Despite the progress in this sense, the performance of high-voltage lithium polymer batteries (HVLPBs) remains insufficient to compete with those of LIBs. One of the reasons is that cycling is usually carried out at low CAM loadings (below 10 $mg \cdot cm^{-2}$) which results in a low cell energy density, even compared to state-of-the-art LIBs. Depending on the specific capacity, a loading of 10 $mg \cdot cm^{-2}$ corresponds to an area capacity comprised between 1.5 and 2 $mAh \cdot cm^{-2}$, whereas for reaching high energy densities, area capacities of 3 $mAh \cdot cm^{-2}$ or higher are required. CAM loading affects the significance of the results, as lithium metal cell performance (especially cycle life and C-rate capability) are heavily dependent on this parameter. Best results, in terms of cyclability, C-rate capability, and operational temperature, are obtained with quasi-solid electrolytes, containing large swaths of solvents or liquid electrolytes [20–28]. These systems have performance comparable to liquid electrolytes, but the use of flammable solvents possibly reintroduces similar safety issues as with standard liquid electrolytes. In comparison, few studies report cyclability data of (mostly plasticized) solid polymer electrolytes with practical CAM loadings (>10 $mg \cdot cm^{-2}$) [29–33].

Another issue regards the scalability of this technology. Few studies show cycling data of HVLPBs in large cell format [22,24,34], owing to the intrinsic difficulties linked to the scaling up process. This is understandable as producing large cells requires large amounts of materials

and specific equipment which is not available to most academic laboratories. However, HVLPB technology has reached a maturity level at which demonstration of scalability is becoming increasingly important. Furthermore, reliable cell abuse tests cannot be performed in small cell format, and these tests are necessary to prove whether there is a real advantage, in terms of safety, in using solid state battery architecture based on polymer electrolytes.

Based on these premises, we aimed at demonstrating scalability, cycling performance, and safety characteristics of HVLPBs. For this, we developed a hybrid ceramic polymer electrolyte (HCPE), composed of a plasticized and cross-linked polyether-based polymer matrix, doped with NASICON $Li_{1+x}Al_xTi_{2-x}(PO_4)_3$ (LATP)-type Li^+-conducting filler particles, and supported on a microporous polyolefin separator. Solid state composite based on Ni-rich NMC-811, conductive additive and Li^+ ion conductive catholyte was used as cathode, and thin, self-standing lithium metal foil as anode. Some results have already been reported in previous publications [35,36]. The transport properties of the HCPE were studied by electrochemical impedance spectroscopy and by solid-state NMR, with a particular focus on the role of the Li^+-conducting ceramic filler. The occurrence of Li^+ exchange between the polymer and the ceramic phase and the participation of the ceramic phase in the long-range charge transport process were proven, especially at high temperatures and high filler concentrations [35]. In another publication [36], we focused on the performance of this system: the HCPE (herein indicated as L1-HCPE) showed excellent mechanical properties and resistance to dendrites growth in Li||Li cells, whereas full cell performance was studied in various formats, from low-loading cathode laboratory cells to high-loading cathode multilayer pouch cells with 1 Ah capacity. The latter showed capacity retention of 80% after 110 cycles and energy density of almost 250 $Wh \cdot kg^{-1}$. In addition, we carried out abuse tests, showing comparable thermal runaway behavior as commercial LIBs with conventional graphite anode.

Herein, we conclude this series of studies, presenting cell performance with an optimized HCPE (L2-HCPE). With respect to the previously reported L1-HCPE, the L2-HCPE was prepared by coating the electrolyte precursor solution on both sides of a microporous separator, with the scope of improving the transport properties, enhancing the wetting of the Li metal anode, and thus the rate capability in full cells. A detailed study on Li||Li symmetric cells, coupled with postmortem SEM analysis, highlighted the effect of the cycling conditions, namely current and capacity, on the Li plating/stripping performance in the contact with the electrolyte. Thereafter, we performed a detailed characterization of multilayer pouch cells, including cyclability test, galvanostatic intermittent titration technique (GITT) analysis coupled with pseudo-2D modeling, electrochemical impedance spectroscopy (EIS) analysis and direct current resistance determination. Most importantly, we performed a detailed postmortem analysis, through which we determined the main root cause of cell failure and carried out overtemperature tests in a closed calorimeter on 1 Ah and 3 Ah cells, providing some useful reference data on the safety characteristics of HVPLBs. This study provides a clear picture of the possibilities and challenges of high-voltage polymer lithium batteries employing polyether-based hybrid ceramic-polymer electrolytes, particularly regarding cycling performance and safety, which can be useful for the further development of this technology.

Experimental section

HCPE preparation and characterization

The composition and preparation process of L1-HCPE were reported in a previous publication [36]. HCPEs are composed of a copolymer of ethylene oxide and propylene oxide (p(EO-*co*-PO) M_w ~800 kg·mol^{-1}), poly(ethylene glycol) dimethyl ether (PEGDME, M_n ~500 g·mol^{-1}, Merck) as polymeric plasticizer and poly(ethylene glycol) diacrylate (PEGDA, M_n ~700 g·mol^{-1}, Merck) as cross-linker. The HCPE sheets were prepared in an argon-filled glove box.

In a typical preparation, the polymer matrix components (p(EO-*co*-PO): 1.04 g, PEGDME: 1.8 g, and PEGDA: 0.76 g), lithium bis(trifluoromethanesulfonyl)imide (LiTFSI, Solvionic, in molar ratio EO:Li = 16, *i.e.*: 1.39 g), and $Li_{1+x}Al_xTi_{2-x}(PO_4)_3$ particles (LATP, Schott, 5 vol%, i.e.: 0.67 g) were mixed overnight in acetonitrile (ACN, 24 mL). The next day, azobisisobutyronitrile (AIBN, Merck, 15 mg) was added as radical initiator to the solution. Thereafter, the solution was further homogenized with a Micro Pulverisette 7 premium planetary (Fritsch), with hermetically sealed 45 mL zirconium flasks, loaded and sealed in an argon atmosphere with 5 mm diameter ZrO_2 beads. The milling time was 20 min and the speed was 250 rpm. The suspension was cast on a Celgard 2500 separator, with a blade gap of 350 µm. The ACN was first evaporated for 3 hours at room temperature, and then at 70 °C, 500 mbar, to complete the cross-linking step. Differently than in the previous paper, a second layer was then coated on the back side of the coated separator. The second cast solution had similar composition to the first one, although without LATP. Processing conditions for the second coating (mixing, casting, drying, curing) were the same, except that no milling and homogenization were performed. Prior to characterization, the membranes were dried overnight under a dynamic vacuum, at room temperature. Final membrane thickness for HCPE characterization and coin cell cycling ranged between 40 and 60 µm, whereas for pouch cell use, the HCPE thickness was reduced to 40 – 50 µm.

The ionic conductivity of the HCPE membranes between 20 °C and 80 °C was measured by electrochemical impedance spectroscopy (EIS) with a Solartron 1260A Impedance/Gain-Phase Analyzer. EIS spectra were collected in the frequency range comprised between 32 MHz and 1 Hz, with 20 points per decade, and with a signal amplitude of 20 mV. The measurements were carried out in coin cells CR2032, with stainless steel electrodes. The measurement was repeated on three replicate cells. The temperature was controlled with a Binder KB23 incubator. The ionic conductivity was calculated with equation 1):

$$\sigma = \frac{1}{R}\frac{L}{A} \quad (1)$$

where R is the bulk electrolyte resistance, L is the membrane thickness, and A is the electrodes surface area and. The latter was measured after the experiment, with a digital micrometer.

The Li^+ transference number (T^+) at 60 °C was determined by potentiostatic polarization method, coupled with EIS, with a BioLogic VMP3 potentiostat. Three Li||Li coin cells were subjected to a potentiostatic polarization with amplitude of 10 mV for 20 min. The resulting current was recorded at a frequency of ten points per second in the first minute, and then of one point per second. EIS spectra were collected before and after the polarization, after 1 h relaxation. The measurement was repeated six times on each cell, by alternating polarizations of +10 mV and −10 mV. The transference number was then calculated by applying equations 2) [37] and 3) [38].

$$T_{BV}^{+} = \frac{I_{SS}}{I_0}\frac{(\Delta E - I_0 R_0)}{(\Delta E - I_{SS} R_{SS})} \quad (2)$$

$$T_{Wat}^{+} = R_1/(\Delta E/I_{SS} - R_{SS}) \quad (3)$$

where I_0 and I_{SS} are the initial and steady-state currents, respectively, ΔE the applied constant voltage, R_1 the high-frequency resistance in the EIS spectra, and R_0 and R_{SS} are the interface resistances, collected before and after the potentiostatic polarization, respectively. The final reported value was the average of eighteen measurements (three replicate cells, six measurements for each cell).

The Li/HCPE interface resistance at 60 °C was determined from the EIS spectra performed during the transference number experiments, with equation 4):

$$R_{int,Li} = \frac{R_2 A}{2} \quad (4)$$

where R_2 is the low-frequency resistance of the EIS spectra and A is the electrodes area.

The restricted diffusion coefficient (D) at 60 °C was determined by recording the voltage relaxation at the end of each potentiostatic polarization and by applying equation 5) [39]:

$$D = -b\frac{L^2}{\pi^2} \quad 5)$$

where b is the slope of ln$E$ vs. time during the relaxation step.

The oxidative stability of the HCPE membranes at 60 °C was studied by linear sweep voltammetry (LSV), in stainless-steel (SS)||Li coin cells. LSV were performed at a scan rate of 0.1 $mV \cdot s^{-1}$ between the open circuit potential and 6.0 V *vs.* Li/Li^+.

Morphology and elemental composition of HCPE cross-sections were obtained by ion milling technique (Hitachi 4000 Plus ion milling) and further studied by FESEM-EDS (APREO 2 S HiVac FESEM) equipped with a Thermo Scientific Windowless EDS detector. HCPE samples were transferred between the glovebox, the ion milling and the SEM, under argon atmosphere, with a transfer device. Cross-sectioning was performed at −70 ºC with a cryogenic module.

For plating-stripping tests, thin lithium metal film discs (40 µm-thick, 14 mm diameter, Hydro-Quebec) and HCPE discs as separators (80 µm-thick, 16 mm diameter) were assembled into CR2032 coin cells. The three layers were stacked in two steps, first by laminating the lithium on a piece of HCPE, then by performing a second lamination by fixing the second lithium on the other side of the HCPE. The ensemble was inserted into the coin cell case. The components were assembled in a glove box filled with argon (O_2 < 0.1 ppm, H_2O < 0.1 ppm). The coin cells were characterized electrochemically with a BioLogic VMP3 potentiostat.

Post-mortem cross-sections of the Li||Li cells were analyzed using two scanning electron microscopes (SEM), namely a TESCAN Lyra 3 and a Hitachi SU-7000. The elemental composition was obtained using an Oxford Instruments Extreme windowless energy dispersive spectrometer (EDS). The windowless EDS detector detects the Li Kα X-ray signal of the Li metal [40]. The samples were embedded in a vinyl polysiloxane resin (3M ESPE Express 7301T) and the cross-sections were prepared using a Leica RM2265 cryo-microtome in an

anhydrous chamber. The samples were transferred from the anhydrous chamber to the SEM by an internal vacuum transfer system. The micrograph and X-ray maps were acquired at an accelerating voltage of 5 and 10 kV, a probe current of 500 pA, and a working distance of 9 mm using the Lyra 3 SEM. The cross-sectional surfaces were also prepared using an Ar Ion Milling IM5000 CTC cryogenic ion mill (Hitachi, Japan) with a cooling stand for cross-section milling. The milling parameters were 5 kV ion beam energy for 1:50 h milling time in intermittent mode (30 s beam on and 90 s beam off). The sample was rocked by ±40° at a speed of 5 rpm and at a temperature of -100 °C. The micrograph and X-ray maps were acquired at an accelerating voltage of 5 kV, a probe current of 300 pA, and a working distance of 6 mm using the SU-7000 SEM. Both instruments are in an anhydrous chamber.

Cathode preparation

NMC-811 based positive electrodes contain 76 wt% of NMC-811 as cathode active material, 2.8 wt% of C45 carbon black as conductive additive, and 21.2 wt% of catholyte, as described in [36]. N-methyl-2-pyrrolidone (NMP) was used as solvent, and the slurry was obtained by mixing all components with a mechanical mixer. Positive electrodes were fabricated by casting the slurry on a carbon-coated aluminum foil (Al/C, Gelon). Casting process and cathode post processing were prepared at both laboratory and pilot plant scale, for one side coated electrode manufacturing and double side coated electrode manufacturing, respectively.

For laboratory scale cathode preparation, the slurry was cast using a doctor blade, and NMP was evaporated by drying the cast solution at 60 ºC. Afterwards, to improve the electrochemical performance of the final cathode, electrode strips were compacted by calendaring with a hydraulic roll calendar (DPM Solutions) at ambient temperature, and then hot pressed (Laborpresse - Polystat 200T) at 140 ºC.

For the manufacturing of double-sided positive electrodes at pilot plant level, the slurry was cast on the Al/C foil using continuous roll to roll coating system (Mathis). The obtained positive electrode strips were post processed by calendaring with a roll press (Naknor Electrode Rolling Equipment - LDHY400-N45) at ambient temperature, and hot-pressed (Laborpresse - Polystat 200T) at 140 ºC. These cathode post processing conditions lead to a positive electrode with a nominal area capacity of 2.7 $mAh \cdot cm^{-2}$, calculated with a nominal specific capacity of 180 $mAh \cdot g^{-1}$.

Pouch cell assembly and testing

1 Ah pouch cells were manually assembled by stacking NMC-811 based positive electrodes, hybrid composite solid electrolyte membranes and lithium metal foils negative electrodes. The total cathode active material mass defines the final cell capacity, thus for obtaining a cell with a nominal capacity of 1 Ah, six cathode sheets and seven lithium metal foils were used, with a size of 50 × 60 mm^2. For the cell assembling, first, the positive electrode was wrapped in solid electrolyte membrane and then, the laminated cathode was placed over the negative electrode. This stacking process was repeated consecutively for seven anodes and six cathode sheets. The assembling process is depicted in **Figure S1**. All operations have been performed in a dry room with a dew point of -50 ºC.

Full cell cycling

NMC-811||Li coin cells were assembled with single-side coated cathodes having cathode active material loading of ~6 $mg \cdot cm^{-2}$, corresponding to an area capacity of approximately 1 $mAh \cdot cm^{-2}$. The coin cells were cycled at 60 °C and in the voltage range comprised between 3.0 V and 4.2 V. Initially, a rate capability test was carried out, with two cycles performed at C/20, then five cycles at C/10, C/5, C/3, C/2, and C/1. Subsequently, the cells were further cycled at C/10. Cycling was performed on a Neware battery cycler.

Pouch cell electrochemical performance was studied by summiting it to charge and discharge cycles of 0.1C/0.1C within a cycling range of 3.0-4.2 V at a temperature of 60 °C. To ensure good contact of cell components, testing was carried out under external pressure, placing each cell between two metallic plates and applying a torque of 0.3 Nm (ca. 3 $kg \cdot cm^{-2}$).

Direct current resistance (DCR) of 1 Ah cells was measured by applying short pulses during charge and discharge at specific values of state of charge (SoC), and then by measuring the resulting voltage drop. Specifically, the cell capacity was first determined by performing one cycle at C/10 (referred to the nominal capacity), between 3.0 and 4.2 V. The voltage profile obtained in this cycle was then used to determine the voltages corresponding to 10% SoC intervals. The cell was then charged at C/10 up to the predetermined voltages, at which short negative current pulses of 10 s duration were applied. At both low and high SoCs (for discharge and charge pulses, respectively), a lower pulse intensity was applied, as the cutoff voltage may be reached before end of pulse total duration. In this study, three pulses were used at each SoC, with intensity of C/10, C/5, and C/3 at SoC of 10, 90, and 100%, and of C/5, C/3, and C/2 at the other SoCs. The experiment was repeated during discharge. The voltage drops obtained were then interpolated to obtain the values of DCR at each SoC during charge and discharge.

GITT measurements were performed for the solid-state cells to investigate Li^+ ion diffusion path within the active material particle. A formation cycle at C/20 was completed by each investigated cell prior to GITT measurements. After the formation cycle, a current pulse corresponding to 2% SoC at C/20 rate was applied during charge and discharge steps. The expression of the voltage evolution upon applied current pulse is shown in equation 6) where the term $R \cdot i_n$ represents the voltage drop due to resistance (R) and applied current (i_n) whereas x is the lithiation/delithiation degree [40]. In the equation, stoichiometry at the particle surface is shown by x_s while pre-pulse and post-pulse stoichiometry are shown by x_0 and x_1, respectively. The analytical representation of the diffusion coefficient (D_s) is shown in equation

7) as a function of pulse time (t), maximum Li concentration in the active material (C_{max} [40,41]), lithium surface flux density into the particle (J_s), and electrode potential (E) [41]. The parameters used for calculating D_s are shown in **Table S1**.

$$V = R \cdot i_n + \frac{U_0(x_1 - x_S) + U_1(x_S - x_0)}{x_1 - x_0} \quad 6)$$

$$D_s = \frac{4}{\pi}\left(\frac{j_s}{C_{max}}\frac{\frac{dE_{eq}}{dx}}{\frac{dE}{d\sqrt{t}}}\right)^2 \quad 7)$$

Cell disassembly and postmortem analysis

The multilayer pouch cells were dismantled in a dry room with a dew point of −40 °C. The pouch cells were immersed in liquid nitrogen to freeze the stack, to prepare smaller samples for the laser cross-section. The laser cut was carried out on FIB-SEM Zeiss Crossbeam X550 equipped with a femto-second laser. The cut was performed at 50% of the laser power (100% is equivalent to 10 µJ), with a scan speed of 100 mm·s^{-1}. SEM observations were conducted on the laser cross-section after its transfer under inert atmosphere in a LEO 1530VP Gemini. The area analyzed represents 2 × 3 mm^2.

A laboratory X-ray tomograph (NANOTOM 180S Phoenix, GE Technologies) was used to collect images of the pouch cells, which were fixed to a scanner rotation platform. The scans were acquired with an 80 kV tension and 280 µA current. For each rotation angle, five images were averaged, resulting in total to 3500 images. The region investigated was 24 × 24 mm², with an isotropic voxel size of 11 µm. This is equivalent to 16% of the cell volume, considering the cell dimensions (55 × 65 mm^2).

Safety test

The aim of the abuse tests was to cause thermal runaway by overheating of a fully charged 1 Ah cell (with dimensions of 105 × 82 × 1 mm^3, mass of 16.03 g, resistance of 1.1 Ω). Overtemperature tests are conducted either in an open chamber to observe thermal runaway or in a closed calorimeter to measure the energy and the amount of gas released. In both cases, the cell described above was sandwiched between two copper plates (117 × 80 × 5 mm^3, 830 g each, **Figure S2a-c**). A heating pad was assembled by placing a Ni-Cr wire (0.35 mm diameter, 15 Ω) within two layers of ceramic tape (**Figure S2a**). Then, the pad was placed between the cell and one of the copper plates. A thermal insulation layer was added between the pad and the copper plate, to prevent heat loss during the heating phase. The plates were bolted together at 0.35 N·m, to create a compressed sandwich containing the cell (**Figure S2b**). Finally, this stack was thermally insulated with a fiberglass-textile coating (**Figure S2c**). Six thermocouples were used, two on the cell and two on each copper plate. All the thermocouples were used to calculate the energy released by the cell during thermal runaway.

For the closed calorimeter tests, the whole setup described previously (cell, plates, heating wire, insulation, thermocouples) was introduced into a cylindrical reinforced 900 mL-vessel thermally insulated (DENATEC – 316L stainless-steel – 140 x 90 mm – 200 bars – 600 °C – under air atmosphere, **Figure S2d-e**), pre-heated and maintained at 60 °C for several hours (the resistance dropped to 0.21 Ω at 60 °C), before being slowly charged at 40 mA until reaching full capacity (4.2 V – 1.01 Ah) with an Arbin BT200, always at 60 °C. A pressure sensor (RS Pro – IPSL series – 50 mbar) was added to the vessel and thanks to gas-tight orifices, pressure and temperatures within the vessel were recorded during both charging and abusing steps. The heat release Q_+ (kJ) was calculated from the plate enthalpy using equation 8), where $m_{calorimeter}$ is the mass of the calorimeter (kg), $c_{p,calorimeter}$ is the mean plate specific heat capacity, $\Delta T_{calorimeter}$ is the temperature change of the plate (K), and $Q_{heating}$ is the heating energy applied to the cell (kJ).

$$Q_{+} = m_{calorimeter} \cdot c_{p,calorimeter} \cdot \Delta T_{calorimeter} - Q_{heating} \quad 8)$$

The abuse test itself started with a controlled heating phase from the initial 60 °C with a slope of 6°C min^{-1}. The power injected was finely controlled with a power supply (EA - EL 9080-60 DT - 1200W) and sent to the heating pad until thermal runaway occurred.

Results and discussion

HCPE characterization

The properties and cell performance of hybrid ceramic polymer electrolytes (HCPE) composed of p(EO-*co*-PO) copolymer, PEGDME, PEGDA, LiTFSI, and LATP particles were reported in a previous publication [36]. The proposed HCPE was further supported by a polyolefin microporous separator, to enhance the resistance to lithium dendrites growth. Single-coated HCPE will be considered here as reference and will be further referred to as L1-HCPE. With the aim of improving the interfacial properties with the lithium metal anode and the cell performance, optimized HCPEs were further developed, with similar composition, but in which a second casting was carried out on the backside of the HCPE. The double-coated HCPE is here indicated as L2-HCPE. This second coating aims at improving the infiltration of the polymer conducting phase in the polyolefin separator micropores, and to provide better contact with the lithium metal anode. It was carried out without LATP, to avoid incompatibility issues in contact with the Li metal. SEM images of the L2-HCPE are shown in **Figure S3**. Two layers are clearly discernable, one composite layer containing micrometer-sized LATP particles, with thickness of ~20 µm, and a polymer layer, supported on the microporous separator, with thickness of approximately 25 µm. The SEM images show no residual porosity in the polymer layer, confirming the complete infiltration of the polymer electrolyte in the separator micropores, and no discontinuity at the interface between the two layers, indicating successful preparation of the bilayer electrolyte. The thermo-mechanical properties of the optimized L2-

HCPEs are expected to be similar to those of the single-coated L1-HCPEs [36] and they were not further characterized. The transport properties of the L2-HCPEs, on the contrary, were characterized by EIS and by potentiostatic polarization method coupled with EIS. The ionic conductivity was determined by EIS in symmetrical stainless-steel cells (SS||SS) between 20 °C and 80 °C. The ionic conductivity profiles, compared to those of L1-HCPE, are shown in **Figure 1a**, while a representative EIS spectrum, at 60 °C, is shown in **Figure S4**. At 25 °C, the ionic conductivity is $2.5 \cdot 10^{-5}$ S·cm^{-1}. At 60 °C, the ionic conductivity increases to $1.9 \cdot 10^{-4}$ S·cm^{-1}. The dependence of the ionic conductivity with the inverse of the temperature shows the typical curvature of amorphous polymer electrolytes, indicating that the charge transport process is limited by the segmental motion of the polymer matrix. No discontinuity is observed in the conductivity profile, indicating that the material is amorphous in the explored temperature range. The values of ionic conductivity are slightly higher than those reported for L1-HCPE ($2.3 \cdot 10^{-5}$ S·cm^{-1} and $1.4 \cdot 10^{-4}$ S·cm^{-1} at 25 °C and 60 °C, respectively), which is attributed to the higher ratio of the conducting phase with respect to the polyolefin separator and, possibly, to a better infiltration of the polymer electrolyte in the separator micropores. However, the ionic conductivity profile of L2-HCPE shows higher curvature with increasing temperature, which results in lower ionic conductivity at temperatures >70 °C.

EIS spectra of Li||Li symmetric cells were collected at 60 °C, to determine the Li|L2-HCPE interface resistance, and the Li^+ transference number. From high to low frequencies, the EIS spectra show a large semicircle, followed by a smaller one, and finally a capacitive tail (**Figure 1b**). The high frequency resistance, R_1, is attributed to the bulk HCPE resistance, whereas the two semicircles are associated with the same number of resistances, indicated as R_2 and R_3. The former (R_2) is attributed to the interface resistance between the L2-HCPE and the lithium electrodes, that is the combined charge transfer resistance and SEI resistance. R_3, which was not observed in the spectra of the L1-HCPE, is attributed to resistance of the additional interface

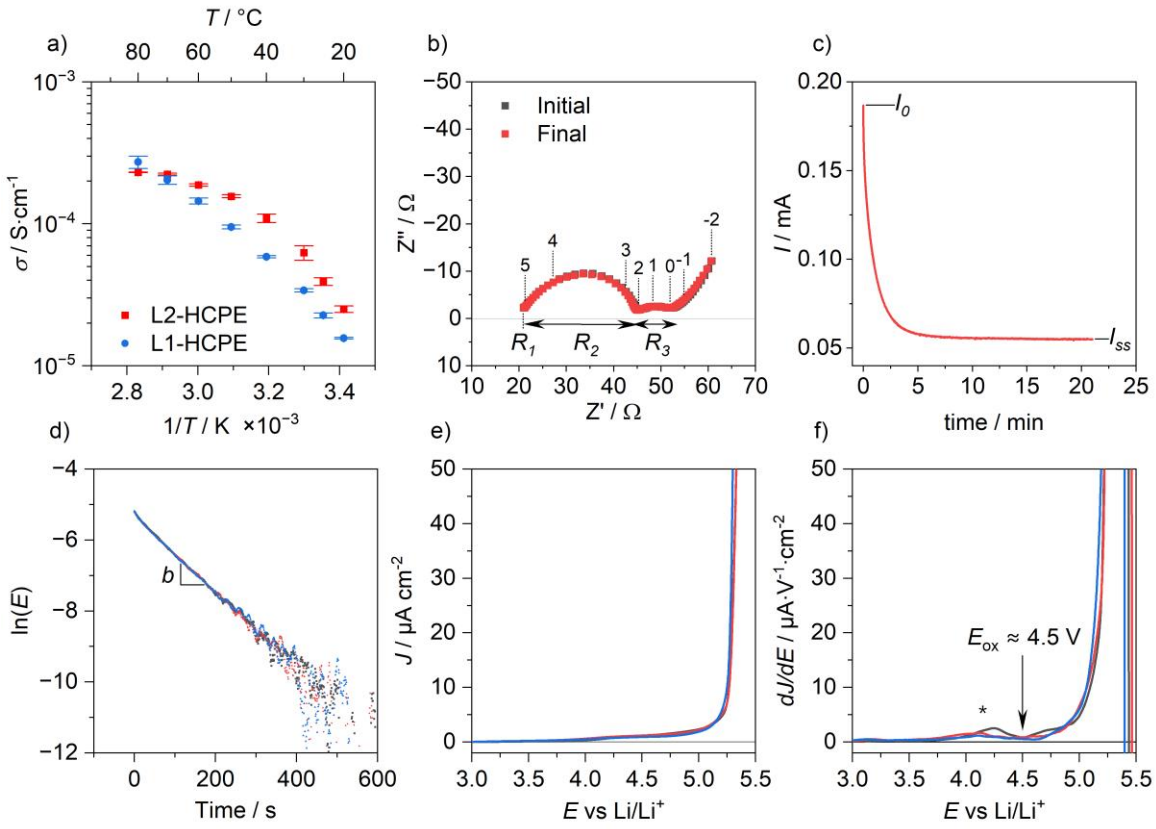

Figure 1. Transport properties of the double coated HCPE (L2-HCPE): a) Ionic conductivity versus the inverse of the absolute temperature, in comparison with single coated HCPE (L1-HCPE, from reference [36]); b) Nyquist plots of the EIS spectra before and after the potentiostatic polarization step, and the superimposed numbers x indicate the frequency, where x = 10^x Hz. The values of real and imaginary impedance are normalized on an area of 1.5394 cm^2; c) typical chronoamperometric profile in Li||Li cells, at 60 °C, at a constant voltage of 10 mV. I_0, Iss, R_1, R_2 and R_3 were used to calculate the lithium transference number T^+ with equations 2) and 3). The interface resistances in equations 2) and 3) is given by the sum of R_2 and R_3. R_2 was used to calculate the interface resistance $R_{int,Li}$ with equation 4); d) evolution of the natural logarithm of the Li||Li cell voltage during the relaxation step after a potentiostatic polarization at 10 mV and 60 °C. The slope b was used to determine the diffusion coefficient, with equation 5); e) LSV profiles of SS|HCPE|Li cells (three cells overlapped), collected at 60 °C and with a scan rate of 0.1 mV s^{-1}; f) first derivative of the LSV profile, showing the first oxidation at 4.0 V and the onset of the final oxidation process at 4.5 V.

layer between the two coated layers in L2-HCPE. This additional interface, internal to the HCPE membrane, arises from the presence of two incoherent crosslinked networks, owing to the separate curing of the two coated layers. Finally, the low-frequency capacitive tail is caused by the buildup of a salt concentration gradient within the HCPE. The interface resistance Li|L2-HCPE, $R_{int,Li}$, was calculated with equation 4) and is 18 Ω·cm^2, considerably lower than that of L1-HCPE (30 Ω·cm^2). The lower value is caused by the presence of an additional polymer electrolyte layer favoring the contact with lithium electrodes. The effect is partially dampened by the presence of the additional resistance R_3 = 10 Ω·cm^2 (6 Ω). Despite this, the total

resistance of Li|L2-HCPE|Li cells is lower than that of Li|L1-HCPE|Li cells, namely 75 Ω·cm^2 (49 Ω) vs. 100 Ω·cm^2. These values are indicative of an improved interface between L2-HCPE and the Li electrodes, but the absolute values cannot be translated to other cell configurations, such as pouch cells, since the different cell pressure will affect the value of the interface resistance.

The EIS spectra, in combination with potentiostatic polarization experiments, were also used to determine the Li+ transference number at 60 °C, by applying equations 2) and 3). The two corresponding values are indicated as T^{+}_{BV} and T^{+}_{Wat}, respectively. Figure 1c shows a typical chronoamperometric profile at a constant voltage polarization of 10 mV and at 60 °C, showing values of I_0 and I_{ss} of 0.187 and 0.055 mA, respectively. The internal cell resistance exclusive of diffusion effects can be calculated by applying Ohm's law to I_0, giving a value of ca. 50 **Ω**, very close to the value determined by EIS (49 **Ω**). As discussed previously, the EIS spectra showed three resistive contributions, R1, R2, R3, from high to low frequency, respectively (**Figure 1**b). For the calculation of T^{+}, the sum of R2 + R3 was used as input for the interface resistance in equations 2) and 3). The value of $T^{+} = 0.14$ is obtained with both equations, close to the value previously obtained for L1-HCPEs.

The presence of R_3 has a negative effect on the long-range salt diffusion within the HCPE. Indeed, restricted diffusion measurements in L2-HCPE provided a diffusion coefficient of $D = 2.2 \pm 0.4 \cdot 10^{-12}$ m^2·s^{-1}, lower than the one obtained with L1-HCPE, for which $D = 3.3 \pm 0.2 \cdot 10^{-12}$ m^2·s^{-1} (**Figure 1d**). It must be noted that this effect was not observed by EIS measurements in the SS||SS cells, as the associated internal interface polarization occurs at relatively low frequencies, namely below 100 Hz (see second semicircle in **Figure 1b**). In SS||SS cells, this polarization is completely masked by the electrode polarization, caused by charge accumulation at the electrodes' interfaces (**Figure S4**). Nonetheless, this additional polarization is possibly related to the larger curvature of the ionic conductivity profile of L2-

HCPE, with respect to L1-HCPE (**Figure 1a**). The additional polarization might be reduced or eliminated by optimizing the preparation process. For instance, a pre-polymerization step could be carried out between the two coating steps, by leaving the membrane for longer time at room temperature, instead of pursuing complete crosslinking at 70 °C. Carrying out complete cross-linking only after the second coating could result in better integration between the two coated layers. For the present stuy, further process optimization was not performed, and following characterization was carried out with the process described in the experimental section.

Finally, the oxidative stability of L2-HCPE was evaluated by LSV (**Figure 1e**). A weak parasitic current is observed between 4.0 V and 4.5 V vs. Li/Li^+. However, the onset for the main oxidation event is at 4.5 V vs. Li/Li^+, in correspondence with the exponential increase of the oxidative current [14], and is attributed to the oxidation of the ethylene oxide units of the polymer host matrix and plasticizer. The onset of the final degradation process can be clearly discerned by analyzing the first derivative of the LSV profile (**Figure 1f**). Given the similar composition of the layer facing the cathode, the oxidative stability is comparable to that of L1-HCPE [36].

Li||Li and NMC-811||Li coin cell tests

In the first part of this study, experiments were carried out with a series of symmetrical cells (Li||Li) to understand the influence of solid electrolyte composition, critical current density (CCD) applied, and the amount of lithium cycled over the lifetime and induced polarization in the cell. It should be noted that, with coin-cells, it is very difficult to have identical cells due to the sensitivity of the interfaces with a very reactive material like lithium metal.

The stability of the Li/electrolyte interface is key parameter for long cycle life of the lithium metal solid-state battery. Then, understanding the aging mechanism of this interface is crucial. In this study, the performance of L1-HCPE (single-side coated) and L2-HCPE (double-side

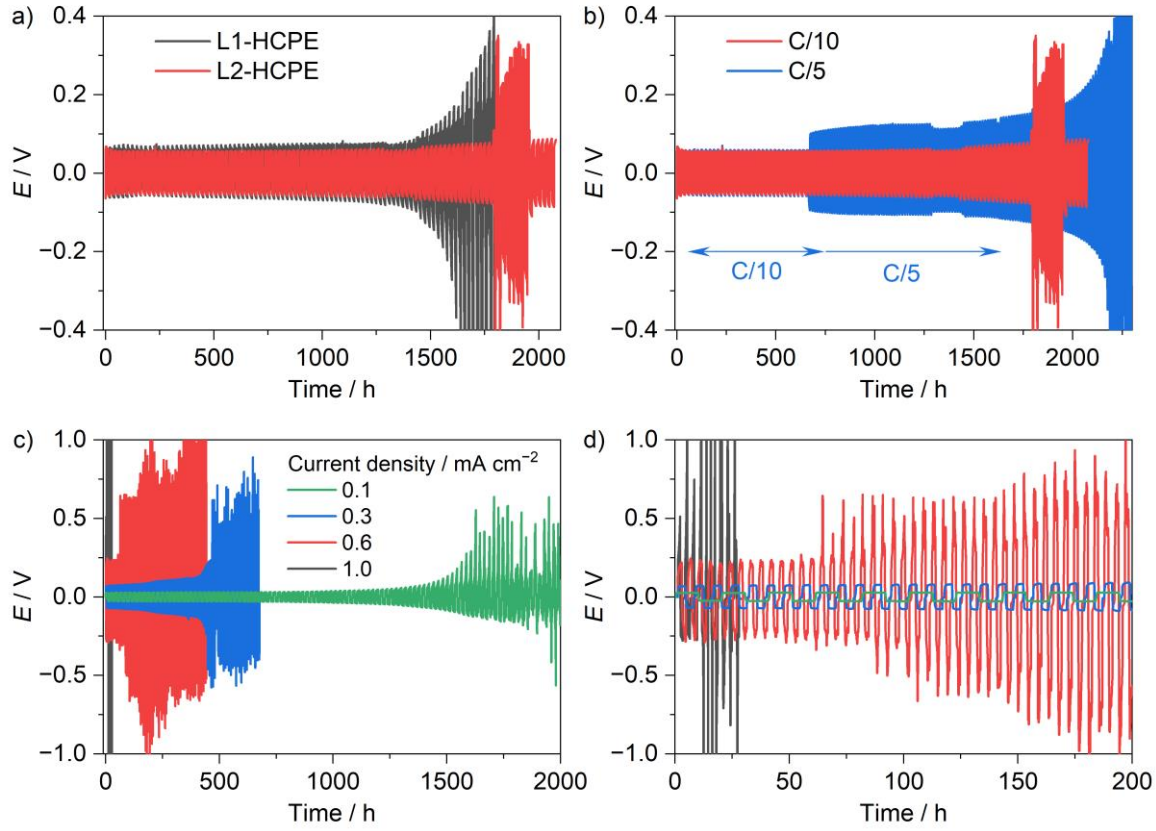

Figure 2. Polarization development of symmetric (Li||Li) cells cycled at 60 °C and at a plated/stripped capacity of 1 mAh·cm^{-2}: a) L1-HCPE and L2-HCPE cycled at a current density of 0.1 mA·cm^{-2} (C/10, for a plated/stripped capacity of 1 mAh·cm^{-2}); b) L2-HCPE cycled at 0.1 mA·cm^{-2} (C/10) and 0.2 mA·cm^{-2} (C/5). Stability of Li|L2-HCPE|Li cells at 60 °C, at fixed capacity of 1 mAh·cm^{-2} and at different current densities: c) whole cycling; d) zoom of the initial 200 h cycling.

coated) were compared, to assess the effect of the second coating on the Li/electrolyte interface. In particular, the impact of the applied current density and of the quantity of lithium metal displaced between the two electrodes during cycling was considered.

In a first set of experiments (**Figure 2a**), symmetrical Li||Li coin cells with the two HCPEs were cycled at 60 °C, at a current density of 0.1 mA·cm^{-2} and at a plated/stripped capacity of 1 mAh·cm^{-2}. As can be seen in **Figure 2a**, good polarization stability for more than 1400 h was achieved for both electrolyte configurations, although the cell with L2-HCPE shows slightly lower polarization. After 1400 h, the polarisation voltage increases with L1-HCPE, whereas it remains stable till 1800 h with L2-HCPE. The cycling in symmetrical cells confirms a higher cycling stability with L2-HCPE, caused by the double-coating improving the interface adhesion with Li metal. Subsequently, the current density was doubled to 0.2 mA·cm^{-2} (C/5)

with the electrolyte L2-HCPE. As shown in **Figure 2b**, a higher applied current density (blue trace at 730 h) results in a higher polarization of ~100 mV. The polarization increases moderately upon cycling up to 1800 h, after which it starts increasing more rapidly. Cell failure coinciding with a steep increase of the polarization is reached at ~2200 h cycling. In all cases, cell failure is possibly related with the exhaustion of the Li reservoir in one of the two Li electrodes.

The impact of current density is very important for the fast charge of the full cell. The impact of cycling conditions on the Li plating/stripping performance of L2-HCPE was further studied by varying the current density while keeping the plating/stripping capacity fixed (**Figure 2c – d**). In general, the expected trends of increasing interface instability and polarization with increasing current densities were confirmed. As shown in **Figure 2c** and **Figure 2d**, the overpotential increases as the applied current density increases. For a fixed capacity of 1 $mAh \cdot cm^{-2}$, the cell was not able to cycle with a current density of 1.0 $mA \cdot cm^{-2}$, owing to the high polarization. By reducing the current density to 0.6 $mA \cdot cm^{-2}$, stable cycling was only achieved for 100 h, before voltage instability appeared. By further reducing the current densities to 0.3 $mA \cdot cm^{-2}$, stability extended to 500 h. At 0.1 $mA \cdot cm^{-2}$ no abnormal voltage fluctuations were observed for more than 1700 h of Li plating/stripping, indicating excellent stability of the Li-interface at this condition. This result clearly shows that the relationship between cycling stability and current density is not linear. Therefore, high current densities generate more complex disturbances at the interfaces. This is a factor that usually has a crucial impact on the cycle life of the full cell.

A post-mortem study of these cells was carried out to better understand the effect of the cycling conditions on the Li/electrolyte interface. The cross-section of the Li|L2-HCPE|Li cell, cycled at 60 °C, 0.1 $mA \cdot cm^{-2}$, and 1 $mAh \cdot cm^{-2}$ showed a significant delamination at the microporous

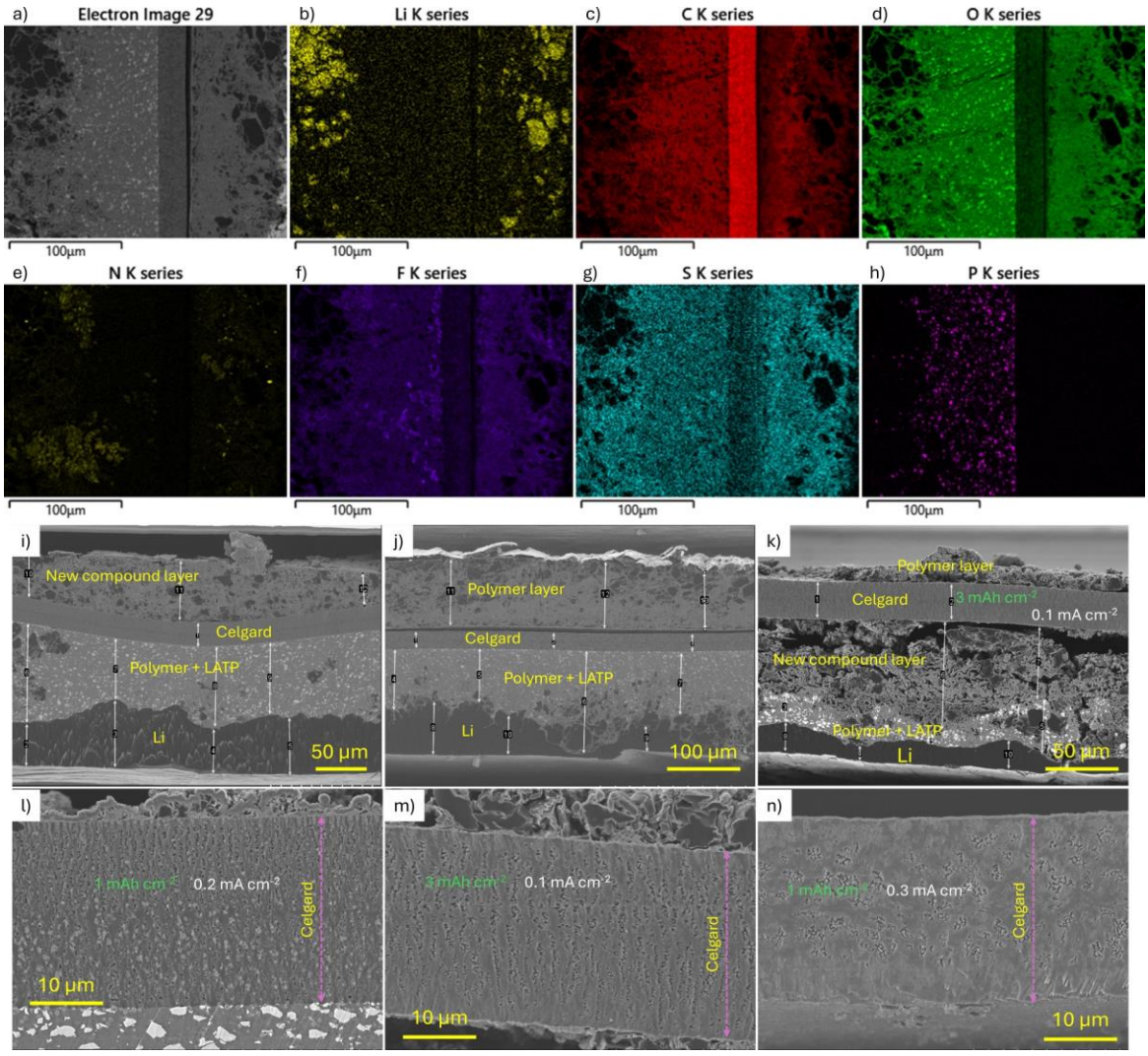

Figure 3. Cross-section SEM images of Li|HCPE|Li cells after cycling at 60 °C at different conditions. a) Li|L2-HCPE|Li cell after cycling at 60 °C at 0.1 mA·cm^{-2} and 1 mAh·cm^{-2}; b – h) mapping of the corresponding chemical elements. N, F, and S derive from TFSI^{-} anion, while P is indicative of the LATP distribution; i) Li|L1-HCPE|Li cell cycled at 1 mAh·cm^{-2}, 0.1 mA·cm^{-2}; j) Li|L2-HCPE|Li cell cycled at 1 mAh·cm^{-2}, 0.2 mA·cm^{-2}; k) Li|L2-HCPE|Li cell cycled at 3 mAh·cm^{-2}, 0.1 mA·cm^{-2}. Cross-section SEM images of the separator layer of Li|L2-HCPE|Li cells after cycling at 60 °C at different conditions: l) 1 mAh·cm^{-2}, 0.2 mA·cm^{-2}; m) 3 mAh·cm^{-2}, 0.1 mA·cm^{-2}; n) 1 mAh·cm^{-2}, 0.3 mA·cm^{-2}.

separator/polymer interface caused by the formation of a new interlayer at the interface between the separator and the polymer film (**Figure 3a – h**). This new interlayer film is formed because of electrolyte decomposition, and these degradation compounds, *e.g.* Li–O–R, LiF and $Li_xS_yO_z$, have already been identified by various works using soft X-ray photoelectron spectroscopy when carbonate, ether-based electrolytes and fluoride salt are used [42,43]. The addition of LATP to the polymer matrix reinforced its mechanical properties, and therefore the latter maintains an intact interface with separator. At the Li/electrolyte interfaces, several

clusters of dead Li are observed. Thus, we can conclude that, at these cycling conditions, the cell failure mode is directly linked to the degradation of the Li/electrolyte interface.

The impact of the applied current density and of the amount of lithium metal cycled were further studied by SEM postmortem analysis. The comparison of the cross-sections images of cells cycled at different conditions is shown in **Figure 3i – k**. These images reveal the major impact of high current density and high cycled capacity on interface integrity. Cross-section SEM was performed on a Li|L1-HCPE|Li cell cycled for 1600 h at 0.1 $mA \cdot cm^{-2}$, and 1 $mAh \cdot cm^{-2}$ (**Figure 3i**). At this mild cycling condition, the interfaces do not show any evident sign of delamination, and relatively few clusters of dead Li are visible on the HCPE side (bottom with respect to the microporous separator). However, a new 30 – 60 μm thick layer is visible on the top side of the separator, which was formed during cycling. This layer, containing several clusters of dead Li, has already been observed in a previous study, on postmortem SEM-EDS analysis of Li|L1-HCPE|Li cells [36], and was attributed to the diffusion of the mobile components of the polymer host matrix during Li plating. The composition of this layer was studied by EDS in reference [36], revealing that it closely resembles the polymer electrolyte phase. Moving from the separator side toward the lithium electrode, a gradual decrease in fluorine content was observed, alongside increases in oxygen and lithium content. This suggests incorporation of metallic lithium into the polymer phase, possibly resulting in mixed ionic and electronic conductivity. The pronounced formation of this compound layer in the single-coated L1-HCPE is likely due to the poor wettability of the non-coated side of the electrolyte with the lithium metal anode, which facilitates the accumulation of these viscous components at that interface. Nonetheless, the relatively good conditions of the interfaces under these mild cycling conditions are consistent with the good cycling stability shown in **Figure 2**. The cross-section SEM image of a Li|L2-HCPE|Li cell cycled at 0.2 $mA \cdot cm^{-2}$ and 1 $mAh \cdot cm^{-2}$ is shown in **Figure 3j**. As in **Figure 3a**, the image shows the two coated layers on both sides

of the polyolefin separator, resulting from the double coating. A slight delamination is visible between the upper polymer layer and the polyolefin separator, as in **Figure 3a**. Several clusters of dead Li are visible on both sides of the polyolefin separator, and the interface between the Li and the LATP-containing side of the HCPE, although coherent, is evidently inhomogeneous. **Figure 3k** shows the cross-section SEM image of a Li|L2-HCPE|Li cell cycled at 0.1 $mA \cdot cm^{-2}$ and 3 $mAh \cdot cm^{-2}$. In this case, the interfaces are severely degraded, with multiple clusters of dead Li in the LATP-containing HCPE layer, and delamination between the latter and the polyolefin separator. Interestingly, in this case a thick, newly formed polymer layer is observed on the same side of the LATP-containing layer, which was the last plated side. This further suggests that the mobile components of the HCPE diffuse together with the Li following the plating direction.

New layers of degradation compounds inevitably form at the interface with the polyolefin separator whatever the cycling conditions, but their thickness varies depending on the cycling applied conditions. This is how the failure mode occurs at the interface level. Also, dead lithium debris is found scattered throughout the polymer matrix, regardless of the separator side. Both sides of lithium/polymer or lithium/polymer-LATP interfaces were found to be very disrupted when the current density or cycled capacity are high (**Figure 3j, k**). These symptoms are more severe when the cycled capacity increases to 3 $mAh \cdot cm^{-2}$ (**Figure 3k**) compared to 1 $mAh \cdot cm^{-2}$ (**Figure 3i**). Consequently, the thickness of lithium films became inhomogeneous due to the disconnection of dead lithium. Additionally, it was found that lithium metal clusters succeeded to pass through the polymer and polymer -LATP films toward the interface with the separator. Despite the delamination of the films at the interfaces, the separators significantly inhibited the growth of lithium dendrites by blocking the spread of metallic lithium, which improves the safety of the cell from internal short-circuit.

Finally, the behavior of polyolefin separator depending on the cycling conditions was investigated. It was found that the morphology of the separator also changed depending on the cycling conditions. The cross-sectional SEM images (**Figure 3l – n**) show the pore filling of the separator as a function of the cycling applied conditions. Clogging is almost complete when cycling conditions are severe. While pores are still visible when the cell is cycled in moderate conditions (1 $mAh \cdot cm^{-2}$, 0.2 $mA \cdot cm^{-2}$, **Figure 3l**), they start getting clogged as the cycled capacity increases (3 $mAh \cdot cm^{-2}$, 0.1 $mA \cdot cm^{-2}$, **Figure 3m**). On the other hand, the pores are almost completely blocked when the current density is three times higher (1 $mAh \cdot cm^{-2}$, 0.3 $mA \cdot cm^{-2}$, **Figure 3n**). Clearly, this behavior is more marked at the interfaces with the polymer films than at the center of the separator. So, it can be concluded that this effect is more sensitive to the current density than to the areal capacity, and that a direct relationship exists with the local transport properties (ionic conductivity, lithium-ion transference number) of the HCPE. We believe that when the ions move from the polymer layer to the polyolefin separator, they experience a slowdown which generates a salt gradient. Indeed, chemical analysis of the blocked areas at the interfaces with the polymer reveals a precipitation of the salt, which is the cause of this blocking of the pores (**Figure S5**). The increase in current density generates a salt gradient which causes its precipitation during cycling, particularly at high current densities, and thus a rapid increase in resistance.

The electrochemical performance of the L2-HCPE was evaluated in NMC-811||Li coin cells with cathode active material loading of $\sim 6\ mg_{NMC\text{-}811} \cdot cm^{-2}$, corresponding to an area capacity of 1.1 $mAh \cdot cm^{-2}$, considering a specific capacity of 180 $mAh \cdot g^{-1}$ (**Figure 4**). Initially, a rate capability test was performed, followed by long cycling at C/10. At C/20, the coin cells delivered specific capacity of ca. 190 $mAh \cdot g^{-1}$, close to the theoretical capacity of NMC-811 (**Figure 4a**). At C/5, the cells still delivered a specific capacity of 150 $mAh \cdot g^{-1}$. Increasing the current density above C/5 resulted in a markedly increased polarization and in a decrease of

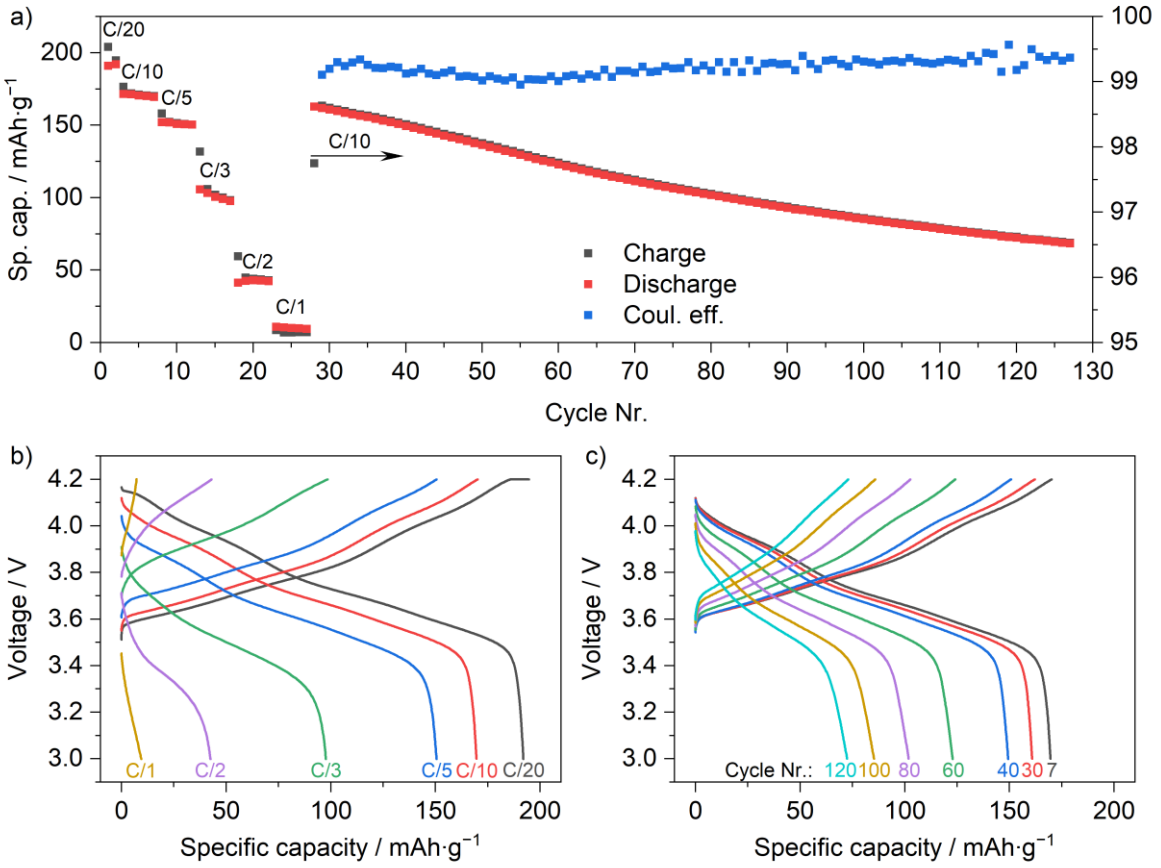

Figure 4. Full cell cycling of NMC-811|L2-HCPE|Li coin cells, at 60 °C and between 3.0 V and 4.2 V, with cathode active material loading of ~6 $mg_{NMC\text{-}811}·cm^{-1}$. a) Specific charge and discharge capacity upon cycling, and coulombic efficiency during long cycling at constant C-rate of C/10; b) voltage profiles at different C-rates; c) voltage profiles at selected cycles during long cycling at C/10.

the delivered capacity, with ca. 100 $mAh·g^{-1}$ at C/3, 40 $mAh·g^{-1}$ at C/2, and only 10 $mAh·g^{-1}$ at C/1 (**Figure 4b**). This marked capacity decrease at high C-rates is the consequence of the sluggish Li-ion dynamics in the polymer electrolyte matrix, and to the increasing polarization at the Li|L2-HCPE interface, as observed in the symmetric cell cycling. After the rate capability test, long cycling was performed at C/10. The cells showed progressive capacity decay, with ca. 40% capacity retention after 100 cycles at C/10. The average coulombic efficiency during long cycling was of 99.2%. The voltage profiles show a progressive increase of the initial polarization, as well as an increasing slope upon cycling (**Figure 4c**), suggesting that capacity decay might be related to increasing of cell resistance upon cycling.

Pouch cell characterization

Cell performance was further evaluated in multilayer pouch cells with relevant configuration, namely having nominal capacity of 1 Ah, cathode active material loading of ~15-16 $mg_{NMC-811} \cdot cm^{-2}$, and lithium thickness of 20 µm per cell (a self-standing 40 µm-thick lithium metal foil for two individual cell). Firstly, pouch cell characterization was performed by determining the direct current resistance (DCR) and the diffusion coefficient by galvanostatic intermittent titration technique (GITT). The DCR at different SoCs was determined by applying short negative pulses of increasing intensity, and by interpolating the resulting voltage drop values, as described in the experimental section. The values of voltage corresponding to each SoC value, determined during the previous cycle at C/10, as well as the current and voltage values during the pulses, are reported in **Table S2** and **Table S3**. The resulting DCR values are shown in **Figure 5a**. During charge, the DCR is almost independent on the SoC (*ca.* 0.3 Ω), only slightly increasing at the extreme SoC values. During discharge, except for the point at SoC 90% which is clearly an outlier, a similar behavior of the DCR as a function of SOC was observed, between SoC 100% and SoC 40% (*ca.* 0.3 Ω as during charge); at lower SoC values, the DCR increases (from 0.3 Ω to 0.5 Ω at SoC 10%), possibly resulting from a more sluggish lithium stripping process at lower cell voltages. Quite interestingly, the cell shows much lower DCR than another pouch cell with single-coated L1-HCPE (**Figure 5a**), indicating that the interface resistance between the solid electrolyte and the lithium electrode has a high impact on the overall cell resistance. A galvanostatic intermittent titration technique (GITT) experiment was carried out to study the kinetic and diffusion properties of the developed system (**Figure 5b**). Solid phase diffusivity of Li (D_S) in the electrodes affects the rate capability of cells as it is a relatively slow process compared to Li^+ diffusion in liquid electrolytes. D_S changes as a function of state of charge (SoC), temperature, and electrolyte concentration [44]. Additionally, the morphology and lattice periodicity of the electrode active

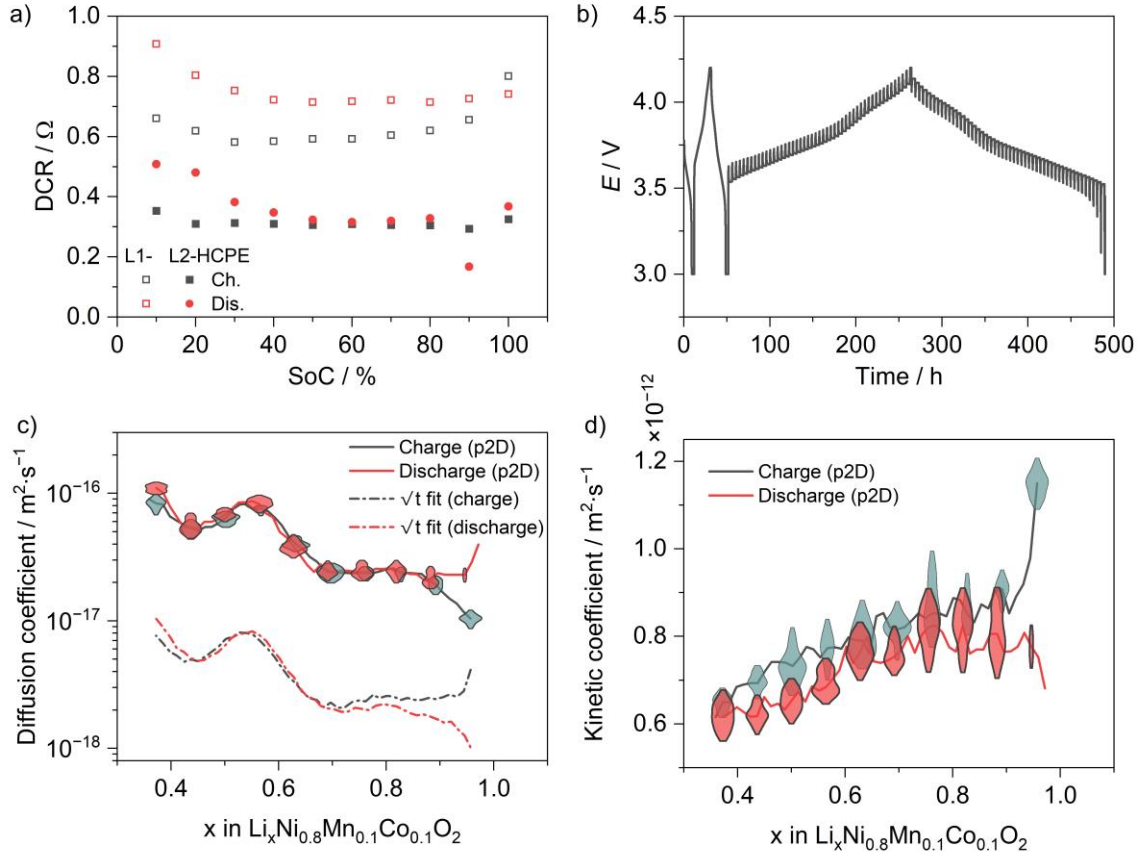

Figure 5. a) DCR at 60 °C of 1 Ah pouch cells, as a function of the SoCs; b) voltage profile during the GITT experiment; c) Diffusion coefficient at 60 °C, estimated by p2D approach (solid lines) and the common fit to √t (dot-dash lines); d) kinetic coefficient at 60 °C estimated by the p2D approach.

material is shown to affect Li^+ diffusivity in solid-state cells. For instance, single-crystalline $LiNi_{0.5}Mn_{0.3}Co_{0.2}O_2$ (NMC-532) exhibits 6 – 14 times higher D_S values compared to its polycrystalline counterpart under the same conditions [45]. GITT method, utilizing time-domain voltage response produced by short current pulses between long relaxation periods, is a common approach to calculate D_S in half cell configuration. Since Li metal electrode produces a negligible overpotential, the major transport limitation occurs due to diffusion of Li in the positive electrodes in Li-ion cells when standard liquid electrolytes are used [46]. In the case of HCPE and all solid-state electrolytes, restrained Li transport is observed at high current rates, whereas the influence of ion transport across the polymer or solid-state electrolyte interfaces are less pronounced at lower current rates [46]. Since GITT measurements consist of low currents applied for a limited time between rather long relaxation times, a concentration

equilibrium could be achieved under the driving force from concentration difference and electric fields. Thus, a careful analysis should be executed to determine whether the Li^+ transport in HCPE limits overall Li diffusivity in the cells or the major kinetic limitation is the solid phase diffusivity of Li in the bulk of the positive electrode.

As ionic transport in the cathode of SSBs tends to be more sluggish than in the case of liquid electrolytes, the GITT experiment may not fully succeed in isolating the solid-phase diffusion as the sole limiting mechanism. This can lead to underestimations of the diffusion coefficient, as discussed by several sources. [41,47].

To assess this possible limitation of transport of ionic phases during the GITT experiments, a more detailed estimation of the solid diffusion coefficient in the solid was performed, by using a full model including ionic and solid diffusion processes as well as charge transport and kinetics. Thus, each of the GITT pulses are simulated using a pseudo-2D (p2D) approach (with a planar Li negative electrode) to account for both the solid and ionic transport limitations. A detailed description of the p2D model approach is reported by Doyle *et al.* [48,49]. Using inverse-modelling, the effective solid diffusion coefficient of the active material in the electrode can be determined by fitting the model to the GITT experimental results.

The summary of parameters used for the model is provided in **Table S1**. The transport properties of the catholyte were determined by the same methods applied above for the solid electrolyte. The parameters obtained for the catholyte were 0.26 $S \cdot m^{-1}$ and 0.1 for the ionic conductivity and Li^+ transference number, respectively. Moreover, the lithium-ion diffusion coefficient was estimated based on the conductivity and transference number using Nernst-Einstein relation, and the resulting value was $2.2 \cdot 10^{-12}\ m^2 \cdot s^{-1}$. The catholyte tortuosity was estimated based on the data presented by Minnmann *et al.* [50], resulting in a value of 7.5. Finally, the volume fraction of catholyte and the initial concentration of lithium ions in the catholyte were estimated based on the electrode composition.

The optimization algorithm used for the parameter estimation was an extended genetic ant colony optimization algorithm (GACO) [51], and the optimization function was the root-mean squared error (RMSE) between the simulated and measured voltage for each of the pulses. For this approach, the fitting parameters were the kinetic coefficient (representing charge transfer resistance of the positive active material) and the solid diffusion coefficient, both of which were assumed constant for each pulse. Thus, the influence of kinetics is limited to the initial voltage change in the pulse, whereas transport and open-circuit potential evolution will correlate with the rest of the pulse. Note that each pulse was simulated individually so that the results are a function of lithium stoichiometry in the material.

The results of the fitting are shown in **Figure 5c**, together with the diffusion coefficient obtained by the more common approach of fitting to $\frac{dV}{d\sqrt{t}}$. The kinetic coefficient, as a function of the lithiation degree, is shown in **Figure 5d**, and the open circuit potential in **Figure S6.** The data from the p2D simulation are represented by the median result of the population of solutions with a RMSE within 0.1 mV of the optimal solution (corresponding to the resolution of the measurement). The shaded area corresponds to the population distribution within such range. When comparing the methods, the values from the full model led to higher diffusion coefficients (around an order of magnitude). Nonetheless, the values obtained for this analysis are still lower than those reported for similar cathode active materials in literature. This is attributed to the present approach not capturing interfacial potentials between catholyte/CAM particles or catholyte/solid electrolyte due to the different activity of the Li^+ ions in the different media. Thus, although the direct determination of the effective solid diffusion coefficient is difficult, it opens the possibility to explore specific modelling approaches to simultaneously estimate the potential effect of such interfaces in the GITT experiment.

Despite being an established technique, D_S values obtained by different GITT methods vary in literature for similar active materials even when a state-of-the-art liquid electrolyte is used.

Shen *et al.* reported a least squares (LS) GITT method and calculated D_s values of 10^{-14} – 10^{-16} $m^2 \cdot s^{-1}$ for NMC electrodes in Li-ion cells showing two orders of magnitude difference with commonly used techniques [44]. Lou *et al.* reported D_s values of $1 – 5 \cdot 10^{-16}$ $m^2 \cdot s^{-1}$ for polycrystalline NMC-622 electrodes (R_p: 10 µm) in an all-solid state Li battery [46]. Moreover, Wang et al. calculated D_s values of $2 – 3 \cdot 10^{-15}$ $m^2 \cdot s^{-1}$ for polycrystalline crystal NMC-532 electrodes in an all solid-state Li battery whereas its single crystal counterpart showed an order of magnitude faster Li diffusion [45]. In this work, we report D_s values at 60 °C in the range of 10^{-16} and 10^{-17} $m^2 \cdot s^{-1}$ for single crystalline NMC-811 electrodes (R_p: 2 µm), calculated by a detailed p2D method that includes the effect of HCPE. The use of a traditional calculation method (with equations 6 and 7), without considering the transport parameter of the HCPE and catholyte, results in values of D_s lower by an order of magnitude. In both cases, the D_s values calculated for the lower lithiation degrees ($x < 0.3$) are excluded since GITT methods are known to be inaccurate in this interval [44]. The low D_s values reported here, compared to the values reported in literature for similar active materials [44,46,52] are attributed to diffusion limitation at the interface between cathode active material and catholyte and between catholyte and HCPE, which are neglected by the p2D model. These interfacial effect (together with the electrochemical activity of Li^+ in the catholyte) will also affect the kinetic coefficient (shown in **Figure 5d**), which is again lower than the values available in the literature for NMC-811 cathodes with liquid electrolytes (which are in the range of $3 – 7 \cdot 10^{-11}$ $mol \cdot m^{-2} \cdot s^{-1} \cdot (mol \cdot m^{-3})^{-1.5}$ [53,54]. The results thus indicate that diffusion limitations in the solid-state ionically conducting phases and at the solid-state interfaces significantly affect the overall cell kinetics. Besides, the order of magnitude difference between the methods compared in this work shows that the importance of transparency and detail in GITT calculations which often lacks in publications. It can be safely concluded that GITT methods can accurately estimate relative change in Li diffusivity as a function of lithiation degree, however, the calculated D_s

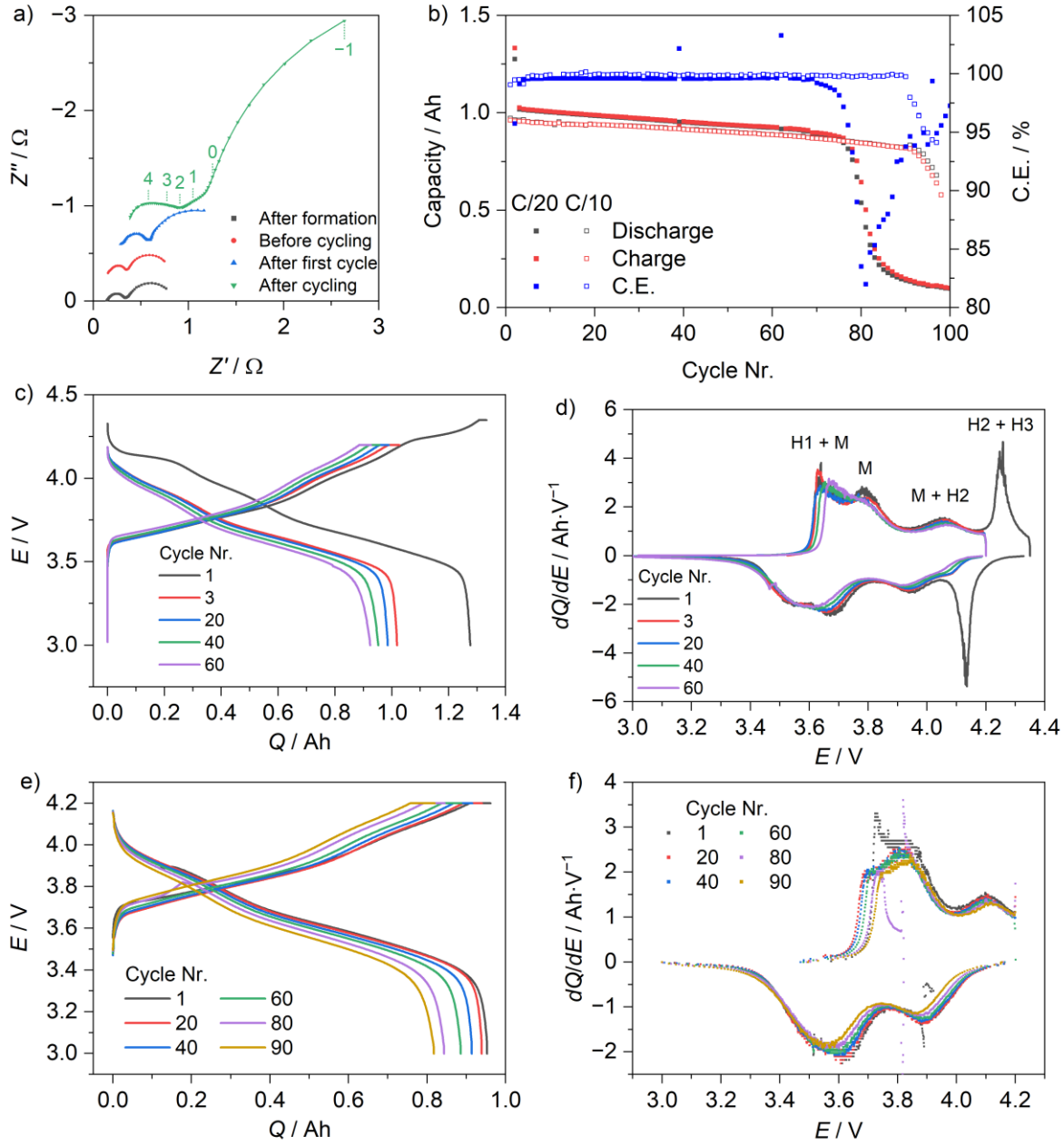

Figure 6. Cycling performance of 1 Ah pouch cells at 60 °C and with an initial pressure of 3 kg·cm^{-2}. a) EIS spectra of the 1 Ah cell, collected after formation, after the first cycle, and after cycling at C/20 (a cumulative vertical offset of −0.3 Ω was applied to distinguish the different traces). Dots and lines represent the experimental points and the fitted curves, respectively. The superimposed numbers (x) indicate the frequency (f), where $f = 10^x$ Hz; b) Discharge capacity and coulombic efficiency of two cells cycled at C/20 and C/10, between 3.0 V and 4.2 V. The first two cycles of the cell cycled at C/20 were performed between 3.0 V and 4.35 V; c) voltage *vs.* capacity profiles of selected cycles at C/20; d) differential capacity profiles of selected cycles at C/20; e) selected voltage profiles at C/10, until cycle 90; f) selected differential capacity profiles at C/10, until cycle 90.

values should be accepted with a grain of salt until the battery science community agrees on a universally accepted method.

After preliminary DCR and GITT characterization, cycling tests on 1 Ah pouch cells were carried out at C/20, coupled with EIS analysis. After formation, and prior to the cycling, the cells were stored at 30% SoC (based on the nominal capacity). Subsequently, EIS spectra were collected, then cells were fully discharged at C/20 to 3.0 V. Thereafter, a cycle at C/20 in the voltage range between 3.0 V and 4.35 V was performed, to determine the whole cell capacity and energy, and another EIS spectrum was collected. The EIS spectra collected after formation, before cycling, and after the first cycle are shown in **Figure 6a**. The first two spectra are similar, despite the second was collected after one month, indicating good cell stability over time. However, the cell impedance increases after the first cycle, from 0.8 Ω to 1.6 Ω. The increase in impedance is partially caused by the different SoC in the initial and final states, 30% and 0% SoC, respectively, although SEI formation and partial degradation at high voltages cannot be excluded, concordantly with a coulombic efficiency of 95.7% in this cycle.

Before cycling, the analysis of the distribution of relaxation times (DRT) showed the presence of four main polarization events with time constants of approximately 10^{-5} s (I, **Figure S7a**, **b**), 10^{-4} s (II), 10^{-2} s (III), and 0.5 s (IV). Equivalent circuit modelling with four RC circuits provided five values of resistance (**Table S4**), one high-frequency series resistance and four resistances associated with the polarization events detected by DRT. The low-frequency resistance, usually associated with the cathode charge transfer resistance [55], represents the largest contribution to the total cell impedance, 0.4 Ω. After cycling, three polarization events were detected by DRT analysis, with time constants of $4 \cdot 10^{-4}$ s, 10^{-2} s, and 1.3 s (**Figure S7c**). In this case, due to noisiness at high frequencies, the DRT analysis was not performed above $6 \cdot 10^{3}$ Hz, so the highest frequency component was not observed. However, the DRT analysis showed an increase in the time constant of the low and middle-high frequency polarization events, which are concordant with an increase of the associated resistances.

The cell capacity and coulombic efficiency during cycling are shown in **Figure 6b**. In the first cycle, the discharge cell capacity and energy were of 1.28 Ah and 4.85 Wh, respectively. These values correspond to a specific capacity of 222 $mAh \cdot g^{-1}$, normalized on the total NMC-811 content, to a specific energy of 358 $Wh \cdot kg^{-1}$, and to a volumetric energy density of 694 $Wh \cdot L^{-1}$, normalized on the stack mass and volume, respectively. Subsequently, the cell was cycled between 3.0 and 4.2 V at C/20, delivering an initial capacity of 1.02 Ah (177 $mAh \cdot g^{-1}$), and thus corresponding to charging up to 80% SoC and discharging to 100% depth of discharge (DoD). The considerable increase in capacity obtained by charging up to 4.35 V is caused by the high-voltage plateau over 4.2 V (**Figure 6c**), which is mainly attributed to the transformation from hexagonal phase H2 to new hexagonal phase H3 of the cathode active material (**Figure 6d**) [56]. In the following cycling, up to cycle 60, the capacity decreased linearly with a capacity fade rate of 0.16% per cycle, while the average coulombic efficiency was of 99.7%. At cycle 60, the capacity retention was of 90.7%, and linear regression of the capacity retention in this range gave a projected 80% value at the cycle 120. Interestingly, the capacity retention was higher in these cells, compared to the coin cells (**Figure 4**), despite the higher cathode active material loading. Better performance in pouch cells, compared to coin cells, was observed also observed in previous works [57,58] and is possibly caused by a higher and more homogeneously distributed internal pressure, as reported by Soulen *et al.* for NMC-532||Li cells with liquid electrolyte [59]. However, the coulombic efficiency started decreasing after cycle 60, resulting in a sudden cell failure at cycle 80. The EIS spectra collected after cycling (green trace in **Figure 6a**) show a substantial increase of the cell impedance, in the mid-frequency region, and especially in the low-frequency region, with the appearance of an additional diffusive contribution in the region between 10^2 and 10^0 Hz. The low frequency resistance accounts for ca. 6 **Ω**, over an overall resistance of almost 8 **Ω**. The increase of the

cell impedance is thus mostly caused by an increase of the cathode charge transfer resistance, and thus to a degradation of the cathode/HCPE interface.

Other cycling tests were performed by cycling pouch cells at C/10, between 3.0 and 4.2 V. Also in these conditions, the cells show similar behaviour, with a first discharge capacity of about 0.96 Ah (corresponding to a specific capacity of 178 $mAh \cdot g^{-1}$, **Figure 6b**), and gravimetric and volumetric energy density values (without casing) of 255 $Wh \cdot kg^{-1}$ and 514 $Wh \cdot L^{-1}$, respectively. The performance is improved with respect to 1 Ah-class pouch cell with L1-HCPE, which showed initial capacity of 0.8 Ah (148 $mAh \cdot g^{-1}$) [36]. Similarly to cells with L1-HCPE, these cells initially show excellent cyclability, with a slight capacity decrease until cycle 90, capacity fade rate of 0.15% per cycle, and average coulombic efficiency of 99.9% between cycle 5 and cycle 90. The capacity retention was 85% at cycle 90. Analysis of the voltage and differential capacity profiles in this range shows a progressive increase of the polarization, probably caused by an increase of the cell impedance (**Figure 6e** and **Figure 6f**). However, from cycle 90 onwards, the capacity and coulombic efficiency drop drastically, leading to sudden cell failure, as observed in the cells cycled at C/20. Analysis of the voltage and differential capacity profiles from cycle 90 to cycle 97 shows only a more rapid increase of the cell polarization, but no voltage noise is observed, which could indicate the buildup of micro shorts (**Figure S8**). Consequently, it is not possible to discern what is the cause of the observed cell failure from the analysis of the cell voltage profiles alone.

The performance of NMC-811|L2-HCPE|Li cells can be compared with previously reported data of similar systems [17,36,60]. For instance, data regarding energy density can be found in reference [60]. In terms of gravimetric energy density, the cells reported in this study outperform LIBs (<300 $Wh \cdot kg^{-1}$) and are in line with other Li metal batteries (LMBs, 300 – 400 $Wh \cdot kg^{-1}$). The volumetric energy density, on the contrary, is comparable to that of LIBs (400 – 700 $Wh \cdot L^{-1}$), and lower than that of other reported LMBs >800 $Wh \cdot L^{-1}$). In most

reported cases, this is due to the lower thickness of the electrolyte, for instance if a liquid electrolyte is used. It must be also noted that it is very challenging for LMBs to reach volumetric energy densities above 1000 $Wh \cdot L^{-1}$ [61].

Data regarding other performance parameters, namely cyclability, rate capability, and operating temperature, can be found also in references [17,36]. Apart from the energy density, which is higher for L2-HCPE, the performance of cells with L2-HCPE are comparable to those of cells with L1-HCPE. Thus, a comparison can be made with similar systems already referenced to in [36], namely cells with dry and plasticized solid polymer electrolytes (SPEs) and with high voltage cathode active materials. Once the cathode active material loading is taken into consideration, the rate-capability and operating temperature are comparable, while the cyclability, so far, is one of the highest reported. Reference [17] summarizes cycling performance of cells with high voltage cathode active materials and SPEs or gel-polymer electrolytes (GPEs). If GPEs are considered, the prospects of SPEs, HCPE included, look less promising. GPEs, containing large swaths of organic solvents, greatly outperform SPEs in terms of cyclability, rate capability, and operating temperature, owing to the far higher ionic conductivity. A similar conclusion can be drawn also for liquid electrolytes [62,63]. Furthermore, strong focus on improving the Li plating-stripping performance, through the optimization of the electrolyte formulation, has resulted in a great increase in cycle life of liquid electrolyte and GPE-based LMBs [64]. In both cases, a trade-off is obtained with safety, due to the use of volatile and flammable organic solvents.

Postmortem analysis

To understand the origin of cell failure, a 1 Ah pouch cell cycled at 60 ºC and at C/10 rate between 3.0 and 4.2 V (**Figure 6**) was disassembled in a glovebox for visual postmortem analysis. **Figure S9** shows the appearance of individual cell components retrieved from the

aged cell. As can be seen from **Figure S9a**, the outer separator layer which was in contact with only the pouch bag remained rather unchanged during cycling while a mild color change on the edges was visible on its back side (**Figure S9c**) which was in contact with the exterior Li electrode (**Figure S9b**). The exterior Li electrode remained bright, like the pristine Li electrode, showing almost no degradation due to cycling. On the other hand, deterioration was notable for the inner Li electrode retrieved from the center of the pouch cell (**Figure S9d**) especially at the edges and corners where islands composed of plated Li accumulated. Unlike the exterior Li, the inner Li could easily be peeled off by applying force on the aged electrode. In addition to the lower integrity of inner Li electrode, the separator placed between Li and the NMC-811 electrode (marked "S" on **Figure S9d**) showed clear transformation during cycling as it appeared bright black instead of whitish. The darkening is attributed to the interpenetration of dead Li into the polymer electrolyte layer upon plating, as observed in the postmortem SEM images of Li||Li cells (**Figure 3**).

Another cell, cycled under the same conditions and showing similar failure mode, was disassembled and subjected to cross-section SEM analysis. Visual inspection showed similar features as the previous cell: the outer lithium electrode was in good conditions (**Figure 7a**), but the inner lithium layers appeared almost completely corroded (**Figure 7b**). The laser-cut cross-section of the cell stack, analyzed by SEM (**Figure 7c**), shows a significant deterioration of the lithium layers, which appear more porous and expanded with respect to the pristine lithium layers. The thickness of the lithium layers is at least 120 µm, reaching in some cases almost 200 µm (**Figure 7d**), whereas the pristine lithium was 40 µm thick. In addition, severe delamination is visible at the lithium anode interface. On the contrary, the cathode layers appear well aligned, with negligible delamination and retained morphology. SEM images at higher magnification (**Figure 7e**) show that delamination occurs mainly at the interface between the porous lithium and the HCPE. The bulk of the lithium layer is composed of a mossy and porous

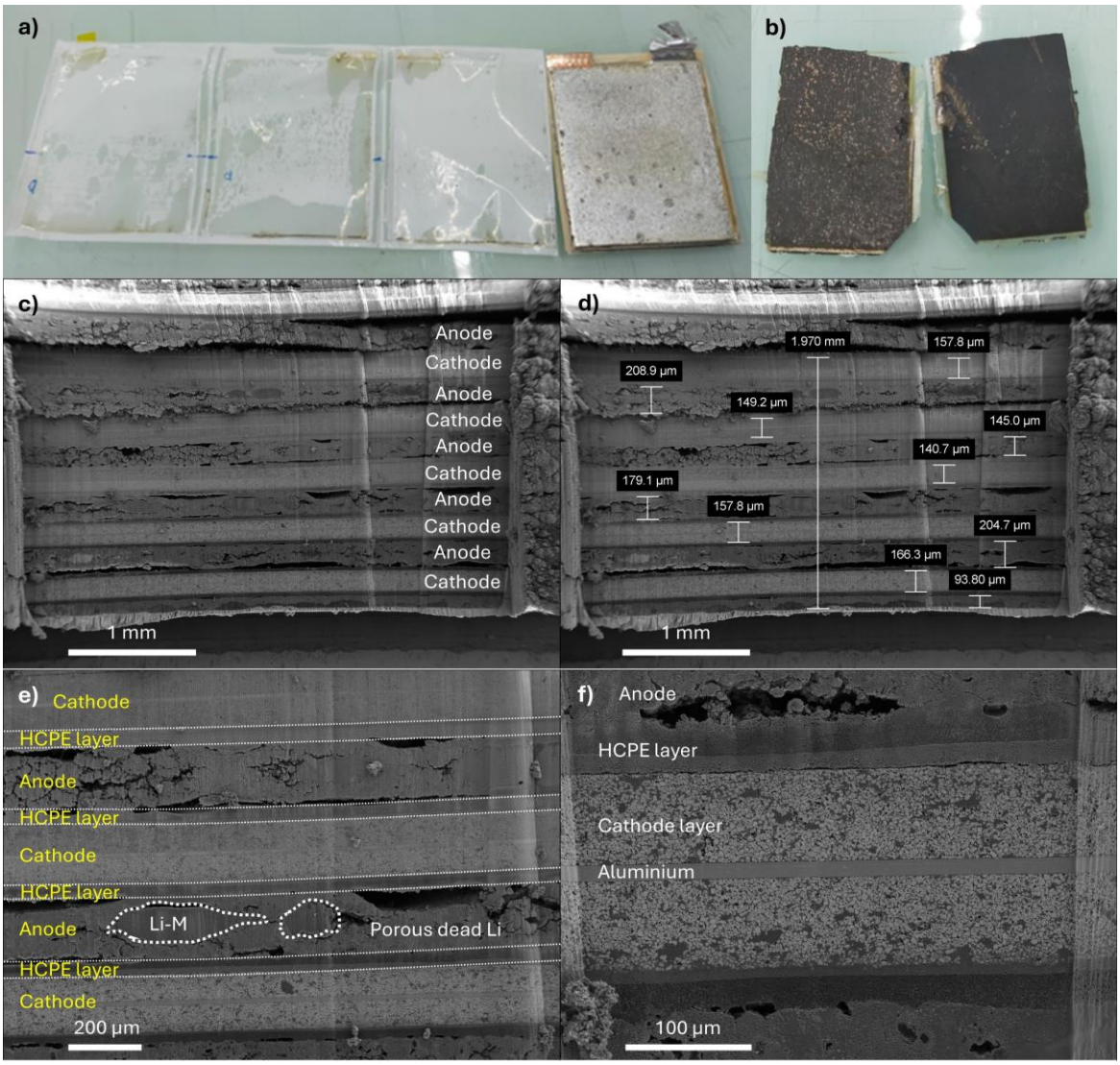

Figure 7. Visual inspection and laser-cut SEM cross-section images of a 1 Ah-pouch cell after cycling. a) External wrapping and external Li metal negative electrode; b) digital image of a completely corroded Li metal electrode (left) and of the cathode layer, covered with the HCPE layer. c – e) SEM images of a laser-cut cell stack cross-section, collected at an acceleration voltage of 5 kV and with a secondary electron detector: c) SEM image of the whole stack, at 26×; d) same images, with the different layer thicknesses indicated; e) SEM image of two individual cell ensembles in the center of the stack, 76×; f) SEM image of a cathode layer, at 258×.

phase, possibly composed of corroded lithium, whereas few isolated clusters of metallic lithium are still visible (shown within dashed lines and indicated as Li-M in **Figure 7e**) [65].

The HCPE/lithium interphase is challenging to study because of the high porosity and the heterogeneous lithium deposits [66]. On the contrary, high magnification SEM images of the cathode (**Figure 7f**) show no mechanical degradation of the cathode. Some pores are visible in the catholyte phase, which can be attributed to ageing. Some cathode active material particles are agglomerated in some areas and are not wetted by the catholyte. There is still good cohesion

between the cathode and the current collector, whereas slight delamination is observed between the cathode layer and the HCPE. The two layers of the HCPE can be still appreciated in **Figure 7f**.

Finally, X-ray tomography was conducted on two cycled 1 Ah pouch cells, to gain further insight into the origin of cell failure. Tomography images of the cross-sections of the two pouch cells are shown in **Figure S10**. The two images are similar, indicating that the cells are mostly homogenous, also considering that the volume analyzed is large and represents 16% of the pouch cell volume. The cathodes, the brightest layers in the figures, are well preserved, with no observed delamination. On the contrary, the anodes (darkest layers) appear deformed and uneven, confirming the high heterogeneity of the Li metal/polymer interphase, as observed by SEM [67].

In conclusion, postmortem analysis indicated that the most probable cause for the observed cell failure is the corrosion and depletion of lithium anodes. Cross-section SEM showed that the lithium metal anodes, after cycling, are completely corroded, with few electrochemically isolated metallic lithium clusters still visible. The cathodes, on the other hand, are well preserved, with no macroscopic delamination nor NMC particles exfoliation.

Safety evaluation

Safety evaluation of 1 Ah and 3 Ah solid state pouch cells were conducted by applying the DO-311 standard in an over-temperature test [68]. This test is one of the most representative because it is minimally influenced by the cells' internal resistance. Over-temperature tests were conducted under two different conditions. The first condition was in an open chamber, allowing for visualization of thermal runaway. The second condition was in a closed calorimeter to measure the energy released during the thermal runaway. To our knowledge, this is the first

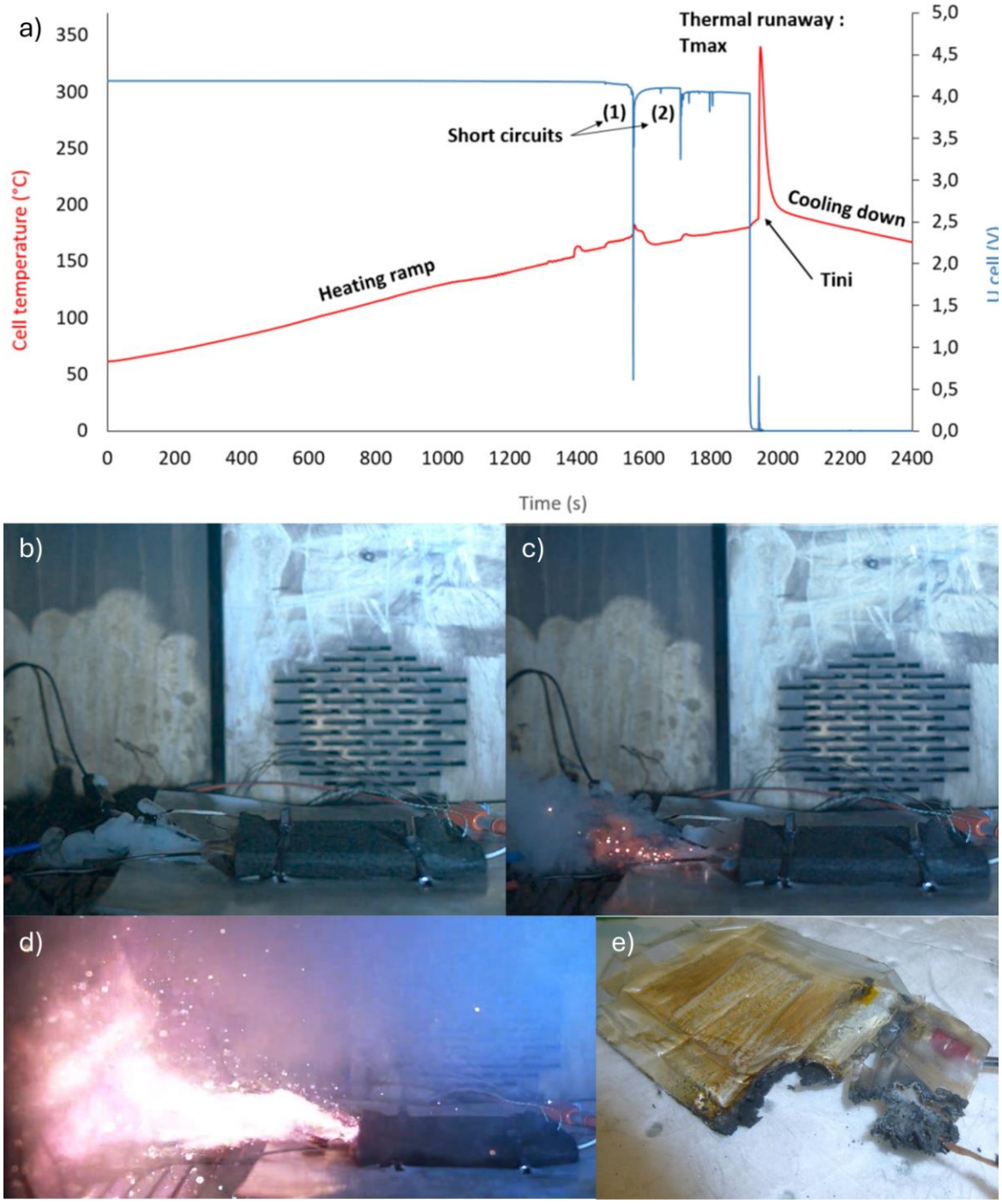

Figure 8. Overtemperature test of a 1 Ah solid-state battery cell at 100% SoC: a) temperature and voltage versus time profile of the cell; b–e) Digital images of the abusive test sequence: b) t = -1 s first plume of smoke; c) t = 0 s, (T = Tini) first sparks; d) wide field of the thermal runaway, (T=Tmax); e) final state of the abused cell.

time that the measurement of energy released by thermal runaway has been performed on this type of lithium metal battery technology.

As shown in **Figure 8a**, the abuse test comprises three steps. Firstly, the cell is artificially heated with a ramp of 6 °C min^{-1} until the thermal runaway initiation temperature (T_{ini}) is

reached. The second part, between T_{ini} and T_{max}, corresponds to the thermal runaway of the cell. Finally, the last part, between T_{max} and T_{amb}, represents the slow cooling of the cell.

The images in **Figure 8b – e** visually present the stages of thermal runaway depicted in the graph in **Figure 8a**. Approximately one second before the thermal runaway (t_0 – 1 s), the cell starts releasing gas. This occurs relatively late compared to LIBs, which generally release gas several minutes before the thermal runaway. At t_0, 1946 seconds after the beginning of the test, the thermal runaway starts with the ejection of incandescent particles (**Figure 8c**). Between t_0 + 1 s and t_0 + 3 s, the runaway reaches its peak. From four seconds after t_0, the thermal runaway significantly slows down, marking the beginning of the cooling phase. The image in **Figure 8e** shows the cell after thermal runaway. It is clearly visible that the reaction has propagated over the entire active surface of the cell. It should also be noted that the cell's mass has decreased by 50%. As shown in **Figure 8a**, after the temperature ramp, thermal runaway is initiated at a temperature of 187 °C. This temperature is consistent with the melting of the lithium metal (180 °C), with the melting of the Celgard 2500 separator (170 °C), and with the destabilization of NMC-811, which generally occurs between 160 and 190 °C [56,69]. It can also be seen from the voltage curve that short circuits were initiated at the 1568th and 1709th seconds of the test. Surprisingly, these short circuits did not lead to thermal runaway, likely because the internal resistance of the cell combined with the resistance of the short circuit was too high. However, the final more pronounced short circuit at the 1916th second ultimately corresponds to the beginning of the thermal runaway.

During the open chamber test, the 3 Ah cell exhibited the same behavior as the 1 Ah cell. **Table 1** presents the values of T_{ini} (initiation temperature of thermal runaway) and d_{TR} (duration of thermal runaway) for these tests. In addition, tests were conducted on 2 cells of 1 Ah and 2 cells of 3 Ah in a closed calorimeter. These tests measured the amount of gas released by the runaway, q_{gas}, as well as the energy released by the runaway, f_E. To facilitate direct

comparison between cells, the values in the table have been standardised according to the capacity of each cell.

Table 1. Data average of thermal runaway characteristic values for 1 Ah and 3 Ah cells. Average of T_{ini} and d_{TR} for the open chamber test and q_{gas} and f_E for the closed calorimeter test.

	T_{ini} / °C	d_{TR} / s	q_{gas} / mol·Ah^{-1}	f_E / kJ·Ah^{-1}
1 Ah	187	3	0.14 ± 0.02	54 ± 7
3 Ah	229	4	0.16 ± 0.02	44 ± 6

Table 1 clearly shows that the 1 Ah and 3 Ah cells exhibit similar values. This validates that, even with small 1 Ah cells, it is possible to effectively evaluate the safety potential of new battery technologies. This is an important point because, for new technologies, 1 Ah is already a significant capacity. Additionally, for the first time to our knowledge, we have measured the energy released during the thermal runaway of Li|HCPE|NMC-811 cells. It is noted that the energy released during the thermal runaway of these cells is slightly higher than that of lithium-ion batteries with liquid electrolyte and graphite anode, with values of 23 and 27 kJ·Ah^{-1} reported by Walker *et al.* [70] and by Charbonnel *et al.* [71], respectively. Likely, the increase in energy released during thermal runaway can be attributed to the presence of excess lithium metal in the NMC-811|HCPE|Li cells, compared to lithium-ion batteries, with an initial Li foil thickness of 20 µm per unit cell in the discharged state. Results thus suggest that the presence of the excess Li metal (additional 1.7 Ah in a 1 Ah cell, with 20 µm-thick lithium) contribute to the energy release during thermal runaway, even with polymer electrolytes. If the energy released is normalized on the total cell charge (considering the lithium metal anode), a value of 20 kJ·Ah^{-1} is obtained, thus close to the one obtained for LIBs.

Conclusions

In this study, we presented the cycling performance, safety characterization, and postmortem analysis, of 1 Ah high-voltage lithium polymer batteries (HVLPBs) with NMC-811-based solid state cathodes, polyolefin separator-supported hybrid ceramic polymer electrolytes (HCPE), and 40 μm-thick self-standing lithium anodes. Firstly, we found that double coating of the HCPE on both sides of the separator enhances the interfacial and transport properties, resulting in improved cycling performance in Li||Li cells. Postmortem analysis, carried out by SEM on cells cross-sections, showed how cycling conditions affects the HCPE ageing upon cycling. Cycling at 3 $mAh \cdot cm^{-2}$ resulted in lithium anode corrosion and in severe degradation of the Li|HCPE interface and HCPE morphology. Full cell performance was first evaluated, at 60 °C, in NMC-811|HCPE|Li coin cells, with areal capacity of 1 $mAh \cdot cm^{-2}$. Cells delivered initial specific capacity of 190 $mAh \cdot g^{-1}$, decreasing to 100 $mAh \cdot g^{-1}$ at C/3, and capacity retention of 40% after 100 cycles at C/10. Electrochemical, cycling, and safety performance were finally evaluated in multilayer pouch cells with 1 Ah nominal capacity, and with extremely high areal capacity of 2.7 $mAh \cdot cm^{-2}$. Cells had direct current resistance of ca. 0.3 Ω at 60 °C; GITT and p2D were used to study the cell kinetics. The 1 Ah pouch cells showed better cyclability than previously tested coin cells, despite the higher loading, likely thanks to the higher and more homogeneous internal pressure achieved in the pouch cells. Cells showed specific energy of 358 $Wh \cdot kg^{-1}$ and capacity retention of almost 90% after 90 cycles at C/10, 80% DoD. Initial capacity and energy density were improved, compared to multilayer pouch cells with single-coated HCPE. However, rapid cell failure was observed, reproducibly, after 80 – 90 cycles. Postmortem analysis revealed that the origin of this failure was lithium metal corrosion, resulting in electrical disconnection of the remaining isolated lithium metal clusters.

Finally, overtemperature tests were conducted on 1 Ah and 3 Ah NMC-811|HCPE|Li cells. These tests showed that the results between 1 Ah and 3 Ah were similar, indicating that it is

feasible to evaluate the safety of new technology using small 1 Ah cells. Furthermore, most of the measured values for evaluating the safety of HCPE cells are comparable to the behavior of commercial high-energy 18650 cells with a liquid electrolyte and conventional electrodes (graphite anode and Ni-rich cathode). This demonstrates the relevance of NMC-811|HCPE|Li cell development for safety. For the first time to our knowledge for HCPE cells, the total energy released during thermal runaway was measured. This energy is higher than that of commercial cells, which is very likely due to the excess lithium metal used in these prototypes, compared to Li-ion batteries. Thus, Li metal content must be further reduced to yield comparable values to lithium-ion batteries.

Altogether, the results showed that the most critical component in HVLPBs is the lithium metal anode, both in terms of cyclability and safety. Continuous consumption of lithium metal is exacerbated at high cycling capacities, which are necessary to achieve high energy densities, and results in early cell failure due to lithium depletion. This effect may be mitigated by introducing SEI-forming additives, to increase the plating/stripping coulombic efficiency, or by switching from self-standing lithium electrodes to Cu-supported Li electrodes, since this will eliminate the sudden loss of capacity by keeping the residual lithium parts connected and therefore electrochemically active. As a drawback, this last strategy would inevitably result in a decrease of the cell specific energy. From the safety perspective, the studied HVLPBs showed similar behavior to commercial lithium-ion batteries. Thermal runaway is initiated at temperatures close to the lithium metal melting point. The released energy is higher than that of commercial LIBs, which is attributed to the presence of lithium metal, representing a considerable charge in addition to the nominal one. When developing high-energy lithium metal batteries, this factor must be carefully considered, even in the presence of a less flammable polymer electrolyte.

Acknowledgements

The authors are grateful to the European Commission for the support of the work performed within the EU H2020 project SAFELiMOVE (grant agreement 875189). Views and opinions expressed are however those of the author(s) only and do not necessarily reflect those of the European Union or CINEA. Neither the European Union nor the granting authority can be held responsible for them. Furthermore, the authors would like to thank all the other partners of the SAFELiMOVE consortium (Schott AG, Umicore, Saft SAS, Ikerlan, Technische Universität Berlin, RWTH Aachen University, ABEE, LCE, and Uniresearch B.V.) for their unvaluable contribution to these research outcomes. In particular, the authors acknowledge Schott AG for developing and providing the LATP electrolyte material, and Umicore for developing and providing the NMC-811 cathode active material. Authors acknowledge Irene Flores and Mónica Cobos (CIDETEC) for the preparation of electrolytes; Jiessei Braccini, Gorka Ortega, Aitzol Oruesagasti, Ion Rementeria (CIDETEC) for the preparation and upscale of positive electrodes; and Irene Flores (CIDETEC) for assembly solid state pouch cells, Gauthier Lefevre, Johannes Ast and Lucile Magnier (CEA) for the laser cut, SEM and tomography.

References

[1] J. Fleischmann, M. Hanicke, E. Horetsky, D. Ibrahim, S. Jautelat, M. Linder, P. Schaufuss, L. Torscht, Alexandre van de Rijt, McKinsey & Company (16 January 2023).

[2] IEA, Trends in batteries – Global EV Outlook 2023 – Analysis - IEA, 2024, https://www.iea.org/reports/global-ev-outlook-2023/trends-in-batteries, accessed 2 April 2024.

[3] K. Shahzad, I. Iqbal Cheema, J. Power Sources 591 (2024) 233888. https://doi.org/10.1016/j.jpowsour.2023.233888.

[4] R. Schmuch, R. Wagner, G. Hörpel, T. Placke, M. Winter, Nat. Energy 3 (2018) 267–278. https://doi.org/10.1038/s41560-018-0107-2.

[5] Vehicle Technologies Office, Batteries: 2022 Annual Progress Report, 2023.

[6] T. Placke, R. Kloepsch, S. Dühnen, M. Winter, J. Solid State Electrochem. 21 (2017) 1939–1964. https://doi.org/10.1007/s10008-017-3610-7.

[7] G. Milazzo, S. Caroli, V.K. Sharma, Tables of standard electrode potentials, Wiley, New York, 1978.

[8] L. Meabe, Itziar Aldalur, Simon Lindberg, Mikel Arrese-Igor, Michel Armand, Maria Martinez-Ibañez, Heng Zhang, Materials Futures 2 (2023) 33501. https://doi.org/10.1088/2752-5724/accdf3.

[9] J. Kalhoff, G.G. Eshetu, D. Bresser, S. Passerini, ChemSusChem 8 (2015) 2154–2175. https://doi.org/10.1002/cssc.201500284.

[10] Q. Zhao, S. Stalin, C.-Z. Zhao, L.A. Archer, Nat. Rev. Mater. 5 (2020) 229–252. https://doi.org/10.1038/s41578-019-0165-5.

[11] S. Dong, L. Sheng, L. Wang, J. Liang, H. Zhang, Z. Chen, H. Xu, X. He, Adv. Funct. Mater. 33 (2023). https://doi.org/10.1002/adfm.202304371.

[12] N. Boaretto, I. Garbayo, S. Valiyaveettil-SobhanRaj, A. Quintela, C. Li, M. Casas-Cabanas, F. Aguesse, J. Power Sources 502 (2021) 229919. https://doi.org/10.1016/j.jpowsour.2021.229919.

[13] F. Croce, F.S. Fiory, L. Persi, B. Scrosati, Electrochem. Solid-State Lett. 4 (2001) A121. https://doi.org/10.1149/1.1380568.

[14] G. Homann, L. Stolz, J. Nair, I.C. Laskovic, M. Winter, J. Kasnatscheew, Sci. Rep. 10 (2020) 4390. https://doi.org/10.1038/s41598-020-61373-9.

[15] S. Kaboli, H. Demers, A. Paolella, A. Darwiche, M. Dontigny, D. Clément, A. Guerfi, M.L. Trudeau, J.B. Goodenough, K. Zaghib, Nano Lett. 20 (2020) 1607–1613. https://doi.org/10.1021/acs.nanolett.9b04452.

[16] Y. Xia, T. Fujieda, K. Tatsumi, P.P. Prosini, T. Sakai, J. Power Sources 92 (2001) 234–243. https://doi.org/10.1016/S0378-7753(00)00533-4.

[17] M.A. Cabañero Martínez, N. Boaretto, A.J. Naylor, F. Alcaide, G.D. Salian, F. Palombarini, E. Ayerbe, M. Borras, M. Casas-Cabanas, Adv. Energy Mater. 12 (2022). https://doi.org/10.1002/aenm.202201264.

[18] S. Xiao, L. Ren, W. Liu, L. Zhang, Q. Wang, Energy Storage Mater. 63 (2023) 102970. https://doi.org/10.1016/j.ensm.2023.102970.

[19] X. Su, X.-P. Xu, Z.-Q. Ji, J. Wu, F. Ma, L.-Z. Fan, Electrochem. Energy Rev. 7 (2024). https://doi.org/10.1007/s41918-023-00204-7.

[20] J. Zhu, J. Zhang, R. Zhao, Y. Zhao, J. Liu, N. Xu, X. Wan, C. Li, Y. Ma, H. Zhang, Y. Chen, Energy Storage Mater. 57 (2023) 92–101. https://doi.org/10.1016/j.ensm.2023.02.012.

[21] G. Zhou, J. Yu, F. Ciucci, Energy Storage Mater. 55 (2023) 642–651. https://doi.org/10.1016/j.ensm.2022.12.020.

[22] S. Zhang, F. Sun, X. Du, X. Zhang, L. Huang, J. Ma, S. Dong, A. Hilger, I. Manke, L. Li, B. Xie, J. Li, Z. Hu, A.C. Komarek, H.-J. Lin, C.-Y. Kuo, C.-T. Chen, P. Han, G. Xu, Z. Cui, G. Cui, Energy Environ. Sci. 16 (2023) 2591–2602. https://doi.org/10.1039/d3ee00558e.

[23] F. Wu, S. Fang, M. Kuenzel, T. Diemant, J.-K. Kim, D. Bresser, G.-T. Kim, S. Passerini, J. Power Sources 557 (2023) 232514. https://doi.org/10.1016/j.jpowsour.2022.232514.

[24] Y. Meng, D. Zhou, R. Liu, Y. Tian, Y. Gao, Y. Wang, B. Sun, F. Kang, M. Armand, B. Li, G. Wang, D. Aurbach, Nat. Energy 8 (2023) 1023–1033. https://doi.org/10.1038/s41560-023-01339-z.

[25] Z. Li, R. Yu, S. Weng, Q. Zhang, X. Wang, X. Guo, Nat. Commun. 14 (2023) 482. https://doi.org/10.1038/s41467-023-35857-x.

[26] X. Dong, A. Mayer, X. Liu, S. Passerini, D. Bresser, ACS Energy Lett. 8 (2023) 1114–1121. https://doi.org/10.1021/acsenergylett.2c02806.

[27] N. Xu, Y. Zhao, M. Ni, J. Zhu, X. Song, X. Bi, J. Zhang, H. Zhang, Y. Ma, C. Li, Y. Chen, Angew. Chem. Int. Ed. (2024) e202404400. https://doi.org/10.1002/anie.202404400.

[28] H. Wang, Y. Yang, C. Gao, T. Chen, J. Song, Y. Zuo, Q. Fang, T. Yang, W. Xiao, K. Zhang, X. Wang, D. Xia, Nat. Commun. 15 (2024) 2500. https://doi.org/10.1038/s41467-024-46883-8.

[29] B. Zhang, L. Chen, J. Hu, Y. Liu, Y. Liu, Q. Feng, G. Zhu, L.-Z. Fan, J. Power Sources 442 (2019) 227230. https://doi.org/10.1016/j.jpowsour.2019.227230.

[30] F. He, W. Tang, X. Zhang, L. Deng, J. Luo, Adv. Mater. 33 (2021) e2105329. https://doi.org/10.1002/adma.202105329.

[31] M. Zuo, Z. Bi, X. Guo, Chem. Eng. J. 463 (2023) 142463. https://doi.org/10.1016/j.cej.2023.142463.

[32] M. Yao, Q. Ruan, S. Pan, H. Zhang, S. Zhang, Adv. Energy Mater. 13 (2023) 2203640. https://doi.org/10.1002/aenm.202203640.

[33] Q. Wu, M. Fang, S. Jiao, S. Li, S. Zhang, Z. Shen, S. Mao, J. Mao, J. Zhang, Y. Tan, K. Shen, J. Lv, W. Hu, Y. He, Y. Lu, Nat. Commun. 14 (2023) 6296. https://doi.org/10.1038/s41467-023-41808-3.

[34] C. Wang, W. Li, S. Ma, M. Zhang, S. Chen, Y. Zhang, H. Xie, L. Cong, J. Energy Storage 77 (2024) 109909. https://doi.org/10.1016/j.est.2023.109909.

[35] N. Boaretto, P. Ghorbanzade, H. Perez-Furundarena, L. Meabe, J.M. Del López Amo, I.E. Gunathilaka, M. Forsyth, J. Schuhmacher, A. Roters, S. Krachkovskiy, A. Guerfi, M. Armand, M. Martinez-Ibañez, Small 20 (2024) e2305769. https://doi.org/10.1002/smll.202305769.

[36] N. Boaretto, L. Meabe, S. Lindberg, H. Perez-Furundarena, I. Aldalur, E. Lobato, F. Bonilla, I. Combarro, A. Gutiérrez-Pardo, A. Kvasha, M. Lechartier, R. Vincent, J. Cognard, S. Genies, L. Daniel, M. Martinez-Ibañez, Advanced Functional Materials (2024) 2404564. https://doi.org/10.1002/adfm.202404564.

[37] J. Evans, C.A. Vincent, P.G. Bruce, Polymer 28 (1987) 2324–2328. https://doi.org/10.1016/0032-3861(87)90394-6.

[38] M. Watanabe, S. Nagano, K. Sanui, N. Ogata, Solid State Ionics 28-30 (1988) 911–917. https://doi.org/10.1016/0167-2738(88)90303-7.

[39] Y. Ma, M. Doyle, T.F. Fuller, M.M. Doeff, L.C. de Jonghe, J. Newman, J. Electrochem. Soc. 142 (1995) 1859–1868. https://doi.org/10.1149/1.2044206.

[40] P. Hovington, V. Timoshevskii, S. Burgess, P. Statham, H. Demers, R. Gauvin, K. Zaghib, Microsc. Microanal. 22 (2016) 84–85. https://doi.org/10.1017/S1431927616001276.

[41] A. Nickol, T. Schied, C. Heubner, M. Schneider, A. Michaelis, M. Bobeth, G. Cuniberti, J. Electrochem. Soc. 167 (2020) 90546. https://doi.org/10.1149/1945-7111/ab9404.

[42] E.K.W. Andersson, C. Sångeland, E. Berggren, F.O.L. Johansson, D. Kühn, A. Lindblad, J. Mindemark, M. Hahlin, J. Mater. Chem. A 9 (2021) 22462–22471. https://doi.org/10.1039/D1TA05015J.

[43] H. Huo, M. Jiang, B. Mogwitz, J. Sann, Y. Yusim, T.-T. Zuo, Y. Moryson, P. Minnmann, F.H. Richter, C. Veer Singh, J. Janek, Angewandte Chemie (International ed. in English) 62 (2023) e202218044. https://doi.org/10.1002/anie.202218044.

[44] Z. Shen, L. Cao, C.D. Rahn, C.-Y. Wang, J. Electrochem. Soc. 160 (2013) A1842-A1846. https://doi.org/10.1149/2.084310jes.

[45] C. Wang, R. Yu, S. Hwang, J. Liang, X. Li, C. Zhao, Y. Sun, J. Wang, N. Holmes, R. Li, H. Huang, S. Zhao, L. Zhang, S. Lu, D. Su, X. Sun, Energy Storage Mater. 30 (2020) 98–103. https://doi.org/10.1016/j.ensm.2020.05.007.

[46] S. Lou, Q. Liu, F. Zhang, Q. Liu, Z. Yu, T. Mu, Y. Zhao, J. Borovilas, Y. Chen, M. Ge, X. Xiao, W.-K. Lee, G. Yin, Y. Yang, X. Sun, J. Wang, Nat Commun 11 (2020) 5700. https://doi.org/10.1038/s41467-020-19528-9.

[47] S.D. Kang, W.C. Chueh, J. Electrochem. Soc. 168 (2021) 120504. https://doi.org/10.1149/1945-7111/ac3940.

[48] M. Doyle, T.F. Fuller, J. Newman, J. Electrochem. Soc. 140 (1993) 1526–1533. https://doi.org/10.1149/1.2221597.

[49] R. Ciria Aylagas, C. Ganuza, R. Parra, M. Yañez, E. Ayerbe, J. Electrochem. Soc. 169 (2022) 90528. https://doi.org/10.1149/1945-7111/ac91fb.

[50] P. Minnmann, L. Quillman, S. Burkhardt, F.H. Richter, J. Janek, J. Electrochem. Soc. 168 (2021) 40537. https://doi.org/10.1149/1945-7111/abf8d7.

[51] M. Schlüter, J.A. Egea, J.R. Banga, Comput. Oper. Res. 36 (2009) 2217–2229. https://doi.org/10.1016/j.cor.2008.08.015.

[52] E. Esen, M. Mohrhardt, P. Lennartz, I. de Meatza, M. Schmuck, M. Winter, E. Paillard, Materials Today Chemistry 30 (2023) 101587. https://doi.org/10.1016/j.mtchem.2023.101587.

[53] C.-H. Chen, F. Brosa Planella, K. O'Regan, D. Gastol, W.D. Widanage, E. Kendrick, J. Electrochem. Soc. 167 (2020) 80534. https://doi.org/10.1149/1945-7111/ab9050.

[54] R. Chowdhury, A. Banerjee, Y. Zhao, X. Liu, N. Brandon, Sustainable Energy Fuels 5 (2021) 1103–1119. https://doi.org/10.1039/D0SE01611J.

[55] S. Seki, Y. Kobayashi, H. Miyashiro, Y. Mita, T. Iwahori, Chem. Mater. 17 (2005) 2041–2045. https://doi.org/10.1021/cm047846c.

[56] H.-J. Noh, S. Youn, C.S. Yoon, Y.-K. Sun, J. Power Sources 233 (2013) 121–130. https://doi.org/10.1016/j.jpowsour.2013.01.063.

[57] Tho Thieu, Elisabetta Fedeli, Oihane Garcia-Calvo, Izaskun Combarro, Juan Nicolas, Idoia Urdampilleta, Andriy Kvasha, Electrochim. Acta 397 (2021) 139249. https://doi.org/10.1016/j.electacta.2021.139249.

[58] Elisabetta Fedeli, Oihane Garcia-Calvo, Antonio Gutiérrez-Pardo, Tho Thieu, Izaskun Combarro, Rodrigo Paris, Juan Nicolas, Hans-Jürgen Grande, Idoia Urdampilleta, Andriy Kvasha, Solid State Ionics 392 (2023) 116148. https://doi.org/10.1016/j.ssi.2023.116148.

[59] C. Soulen, N. Lam, J. Holoubek, P. Liu, J. Electrochem. Soc. 171 (2024) 20535. https://doi.org/10.1149/1945-7111/ad2731.

[60] J. Huang, C. Li, D. Jiang, J. Gao, L. Cheng, G. Li, H. Luo, Z.-L. Xu, D.-M. Shin, Y. Wang, Y. Lu, Y. Kim, Adv Funct Materials 35 (2025). https://doi.org/10.1002/adfm.202411171.

[61] M. Burton, S. Narayanan, B. Jagger, L.F. Olbrich, S. Dhir, M. Shibata, M.J. Lain, R. Astbury, N. Butcher, M. Copley, T. Kotaka, Y. Aihara, M. Pasta, Nat Energy 10 (2025) 135–147. https://doi.org/10.1038/s41560-024-01676-7.

[62] Y. Jie, S. Wang, S. Weng, Y. Liu, M. Yang, C. Tang, X. Li, Z. Zhang, Y. Zhang, Y. Chen, F. Huang, Y. Xu, W. Li, Y. Guo, Z. He, X. Ren, Y. Lu, K. Yang, S. Cao, H. Lin, R. Cao, P. Yan, T. Cheng, X. Wang, S. Jiao, D. Xu, Nat Energy 9 (2024) 987–998. https://doi.org/10.1038/s41560-024-01565-z.

[63] G.-X. Li, V. Koverga, A. Nguyen, R. Kou, M. Ncube, H. Jiang, K. Wang, M. Liao, H. Guo, J. Chen, N. Dandu, A.T. Ngo, D. Wang, Nat Energy (2024) 1–11. https://doi.org/10.1038/s41560-024-01519-5.

[64] G.M. Hobold, J. Lopez, R. Guo, N. Minafra, A. Banerjee, Y. Shirley Meng, Y. Shao-Horn, B.M. Gallant, Nat Energy 6 (2021) 951–960. https://doi.org/10.1038/s41560-021-00910-w.

[65] F. Orsini, A. Du Pasquier, B. Beaudoin, J. Tarascon, M. Trentin, N. Langenhuizen, E. de Beer, P. Notten, J. Power Sources 76 (1998) 19–29. https://doi.org/10.1016/S0378-7753(98)00128-1.

[66] S. Chakraborty, G.K. Sethi, L. Frenck, A.S. Ho, I. Villaluenga, H. Wantanabe, N.P. Balsara, ACS Appl. Energy Mater. 5 (2022) 852–861. https://doi.org/10.1021/acsaem.1c03288.

[67] L. Frenck, P. Lennartz, D.Y. Parkinson, M. Winter, N.P. Balsara, G. Brunklaus, ACS Appl. Mater. Interfaces 14 (2022) 53893–53903. https://doi.org/10.1021/acsami.2c16869.

[68] RTCA, Minimum Operational Performance Standards for rechargeable Lithium battery systems, 2008.

[69] J. Hou, L. Lu, L. Wang, A. Ohma, D. Ren, X. Feng, Y. Li, Y. Li, I. Ootani, X. Han, W. Ren, X. He, Y. Nitta, M. Ouyang, Nat Commun 11 (2020) 5100. https://doi.org/10.1038/s41467-020-18868-w.

[70] William Q. Walker, John J. Darst, Donal P. Finegan, Gary A. Bayles, Kenneth L. Johnson, Eric C. Darcy, Steven L. Rickman, J. Power Sources 415 (2019) 207–218. https://doi.org/10.1016/j.jpowsour.2018.10.099.

[71] J. Charbonnel, N. Darmet, C. Deilhes, L. Broche, M. Reytier, P.-X. Thivel, R. Vincent, ACS Appl. Energy Mater. 5 (2022) 10862–10871. https://doi.org/10.1021/acsaem.2c01514.

Supplementary Information

Table S1. Parameters used for the determination of the solid diffusion coefficient and kinetic coefficient of the cathode active material via GITT and p2D inverse-modelling.

Component	Parameter	Value	Unit	
Solid electrolyte	Ionic conductivity	0.019	$S \cdot m^{-1}$	Measured
	Transference number	0.14	-	Measured
	Diffusion coefficient	$2.2 \cdot 10^{-12}$	$m^2 \cdot s^{-1}$	Measured
	Initial lithium concentration	850	$mol \cdot m^{-3}$	Estimated
	Thickness	82	µm	
Lithium foil	Kinetic coefficient	$3.9 \cdot 10^{-5}$	$mol \cdot m^{-2} \cdot s^{-1} (mol \cdot m^{-3})^{-0.5}$	Estimated [1]
Cathode	Thickness	70	µm	Measured
	Effective electronic conductivity	0.2	$S \cdot m^{-1}$	Estimated
Catholyte	Ionic conductivity	0.26	$S \cdot m^{-1}$	Measured
	Transference number	0.1	-	Measured
	Diffusion coefficient	$1.4 \cdot 10^{-11}$	$m^2 \cdot s^{-1}$	Estimated
	Initial lithium concentration	1000	$mol \cdot m^{-3}$	Estimated
	Volume fraction	0.48	-	Calculated
	Tortuosity	7.5	-	Estimated [2]
Cathode active material	Volume fraction	0.48	-	Calculated
	Particle radius	2	µm	Measured
	Maximum Li concentration	49000	$mol \cdot m^{-3}$	Calculated
	Open-circuit potential	**Figure S6**	V	Measured
	Kinetic coefficient	**Figure 5**	$mol \cdot m^{-2} \cdot s^{-1} (mol \cdot m^{-3})^{-1.5}$	Fit
	Solid diffusion coefficient	**Figure 5**	$m^2 \cdot s^{-1}$	Fit

[1] Mastali, Mehrdad; Farkhondeh, Mohammad; Farhad, Siamak; Fraser, Roydon A.; Fowler, Michael (2016): Electrochemical Modeling of Commercial $LiFePO_4$ and Graphite Electrodes: Kinetic and Transport Properties and Their Temperature Dependence. In *J. Electrochem. Soc.* 163 (13), A2803-A2816. DOI: 10.1149/2.1151613jes.

[2] Minnmann, Philip; Quillman, Lars; Burkhardt, Simon; Richter, Felix H.; Janek, Jürgen (2021): Editors' Choice—Quantifying the Impact of Charge Transport Bottlenecks in Composite Cathodes of All-Solid-State Batteries. In *J. Electrochem. Soc.* 168 (4), p. 40537. DOI: 10.1149/1945-7111/abf8d7.

Table S2. Values used in the determination of the DCR of 1 Ah pouch cells during charge at 60 °C.

SoC / %	E_{OCV} / V	I_1 / mA	E_1 / V	I_2 / mA	E_2 / V	I_3 / mA	E_3 / V
0	3	-43.05	3	-86.1	3	-172.2	3
10	3.68	-43.05	3.623	-86.1	3.606	-172.2	3.577
20	3.74	-172.2	3.648	-287	3.612	-430.5	3.568
30	3.78	-172.2	3.694	-287	3.657	-430.5	3.613
40	3.82	-172.2	3.734	-287	3.7	-430.5	3.654
50	3.86	-172.2	3.776	-287	3.741	-430.5	3.697
60	3.92	-172.2	3.838	-287	3.799	-430.5	3.758
70	3.99	-172.2	3.907	-287	3.872	-430.5	3.828
80	4.06	-172.2	3.978	-287	3.941	-430.5	3.899
90	4.12	-43.05	4.075	-86.1	4.062	-172.2	4.037
100	4.2	-43.05	4.156	-86.1	4.142	-172.2	4.114

SoC: state of charge; $\boldsymbol{E}_{OCV}$: cell voltage corresponding to the specified SoC (determined in the first cycle at C/10); $\boldsymbol{I}_i$: values of current during the pulses; $\boldsymbol{E}_i$: cell voltage during the pulses.

Table S3. Values used in the determination of the DCR of 1 Ah pouch cells during discharge at 60 °C.

SoC / %	E_{OCV} / V	I_1 / mA	E_1 / V	I_2 / mA	E_2 / V	I_3 / mA	E_3 / V
100	4.2	-42.75	4.154	-85.5	4.139	-171	4.107
90	3.92	-42.75	3.91	-85.5	3.91	-171	3.89
80	3.84	-171	3.812	-285	3.775	-427.5	3.728
70	3.76	-171	3.732	-285	3.696	-427.5	3.65
60	3.69	-171	3.66	-285	3.623	-427.5	3.579
50	3.64	-171	3.611	-285	3.573	-427.5	3.528
40	3.6	-171	3.571	-285	3.53	-427.5	3.482
30	3.55	-171	3.518	-285	3.475	-427.5	3.42
20	3.5	-171	3.464	-285	3.411	-427.5	3.341
10	3.44	-42.75	3.439	-85.5	3.438	-171	3.378
0	3	-42.75		-85.5		-171	

SoC: state of charge; $\boldsymbol{E}_{OCV}$: cell voltage corresponding to the specified SoC (determined in the first cycle at C/10); $\boldsymbol{I}_i$: values of current during the pulses; $\boldsymbol{E}_i$: cell voltage during the pulses.

Table S4. Resistance components of the EIS spectra of a 1 Ah cell at 60 °C, after formation (30% SoC), before cycling (30% SoC), and after one cycle (0% SoC). The resistance components were determined by modeling the EIS spectra in **Figure 6a** with a ladder equivalent circuit model, comprising one series resistance and a series of RC elements, whose number was determined by DRT (**Figure S7**). The resistances are listed in order of decreasing frequency.

	R1 / Ω	R2 / Ω	R3 / Ω	R4 / Ω	R5 / Ω
After formation	0.13	0.04	0.16	0.13	0.39
Before cycling	0.15	0.05	0.14	0.11	0.38
After one cycle	0.32		0.25	0.1	1.57

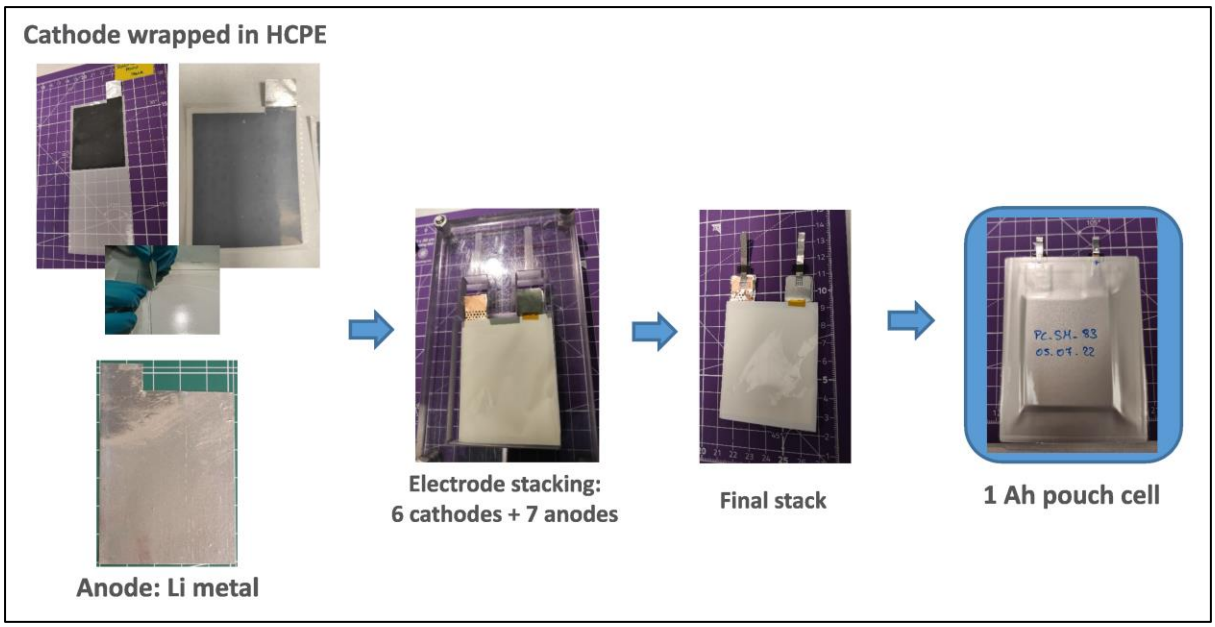

Figure S1. 1 Ah pouch cells assembling process.

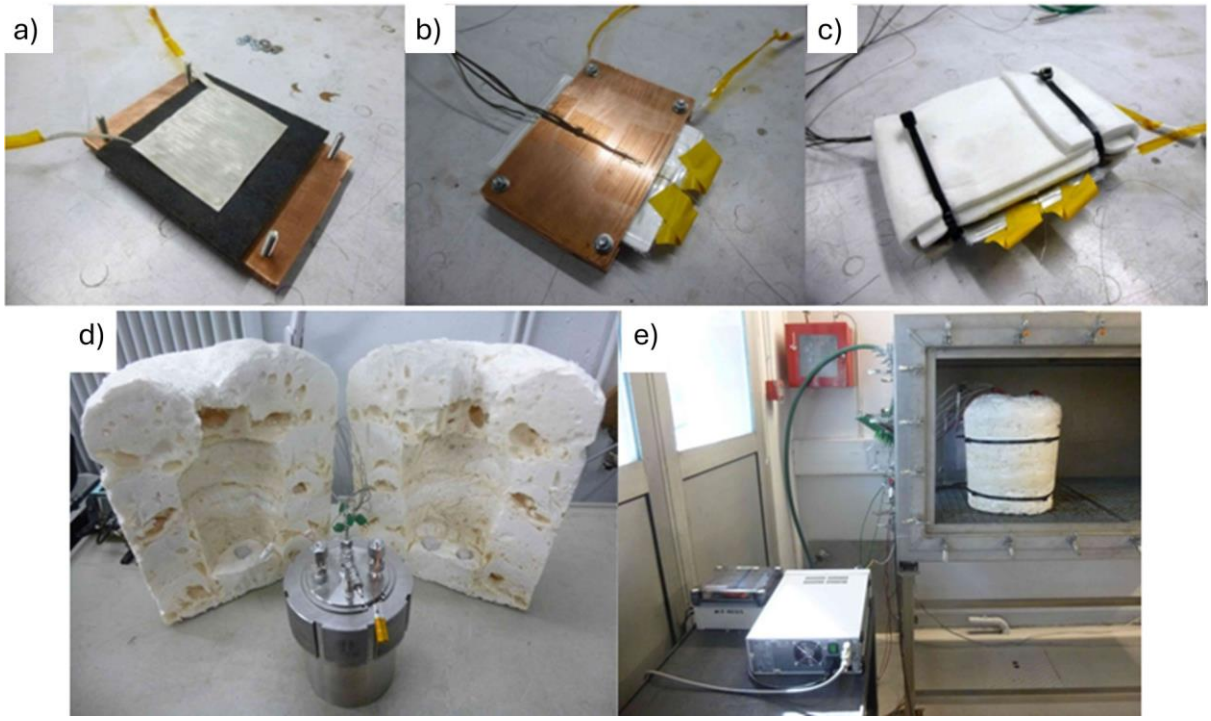

Figure S2. Assembly of the safety test device: a) Cu plate, thermal insulation layer, and heating pad; b) The 1 Ah cell sandwiched between Cu plates with thermocouples; c) final stack wrapped in fiberglass cloth; d) cylindrical reinforced vessel and its thermal insulation; e) whole setup in position for abuse test.

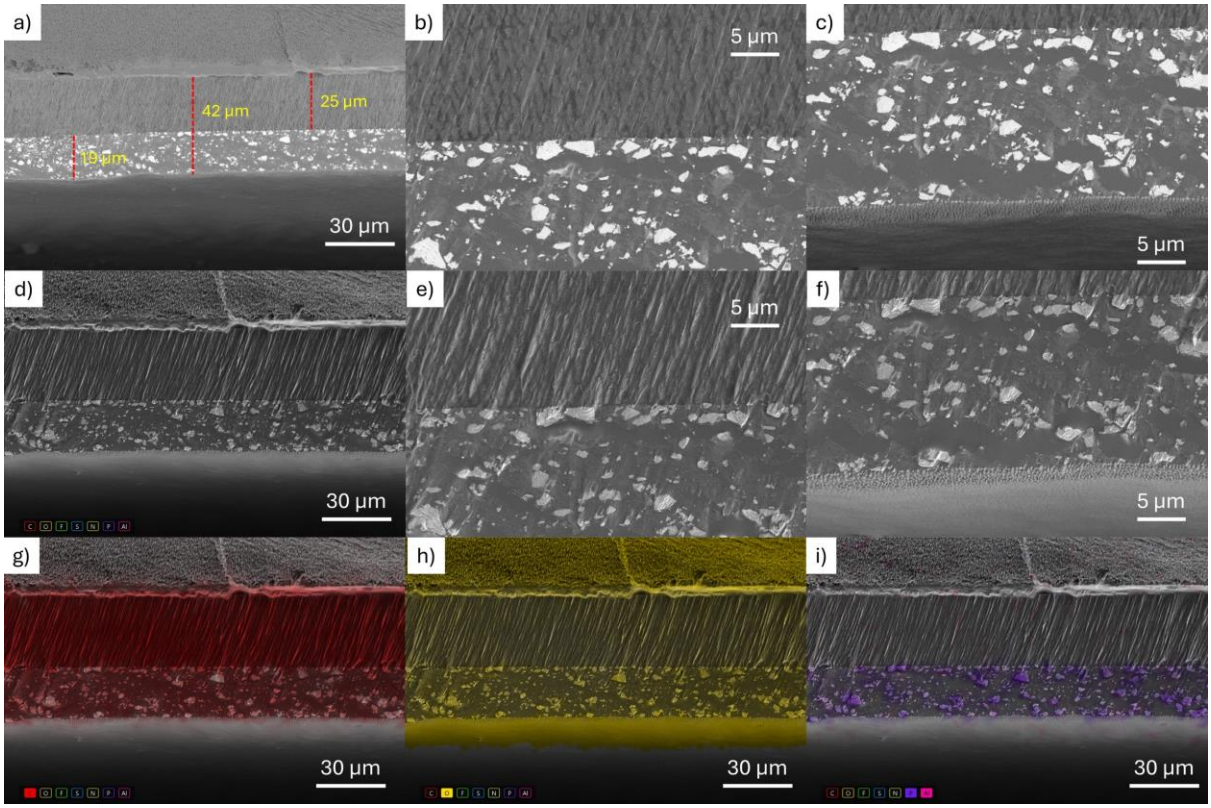

Figure S3. Cross-section SEM images of the pristine L2-HCPE, collected at 2 kV acceleration. a – c) Backscattered electron images collected at: a) 1200× magnification; b), c) 5000× magnification. d – f) Secondary electron images at d) 1200×, e), f) 5000×. g – i) Color SEM collected at 1200×, showing distribution of g) Carbon; h) Oxygen; i) Phosphorus and Aluminum.

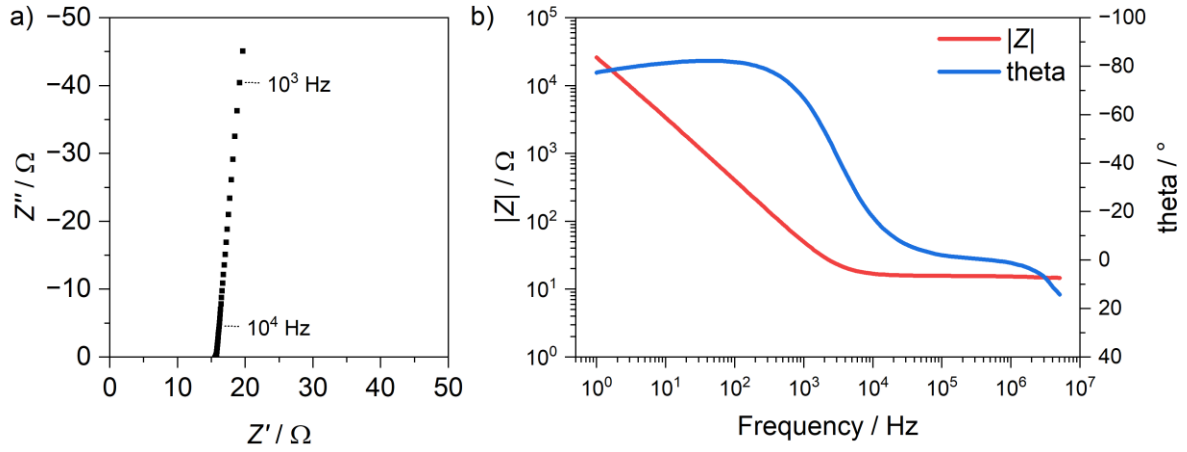

Figure S4. EIS spectra of L2-HCPE in SS||SS cells at 60 °C: a) Nyquist plot; b) Bode plot.

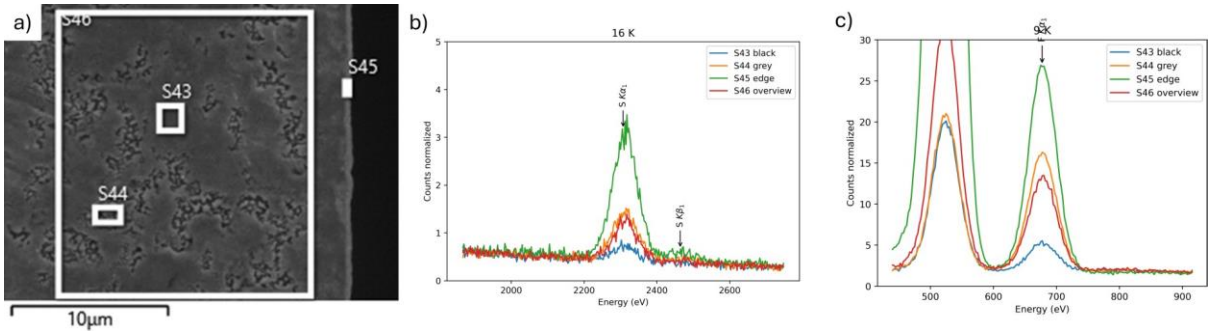

Figure S5. Elemental analysis on the polyolefin separator layer cross-section of the cell cycled at 0.3 mA·cm^{-2}.

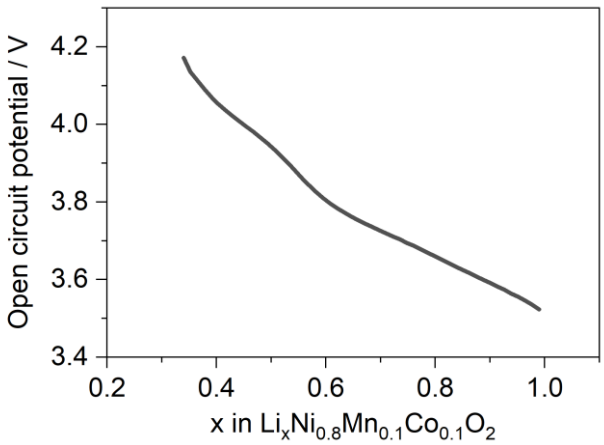

Figure S6. Open circuit potential, as a function of the lithiation degree of NMC-811, during a GITT experiment on a 1 Ah NMC-811|L2-HCPE|Li cell.

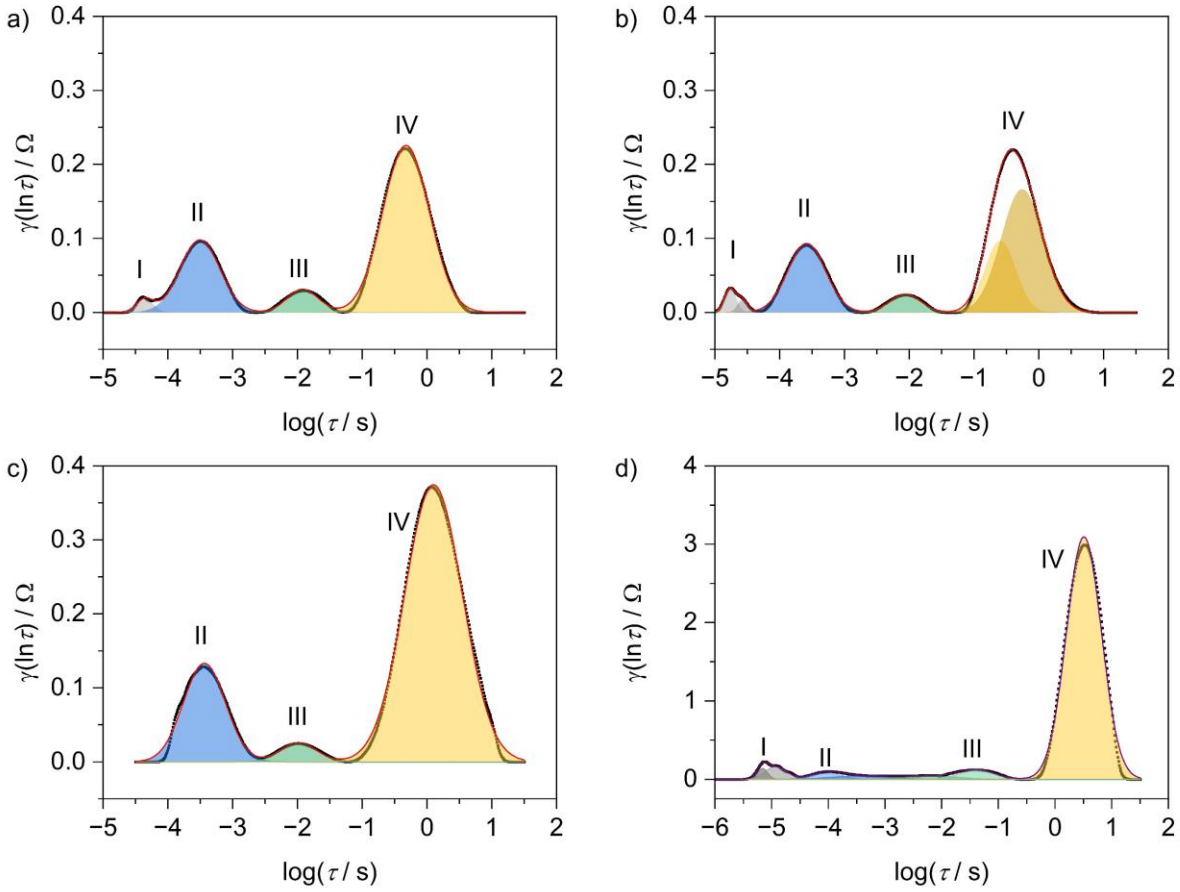

Figure S7. DRT analysis of the EIS spectra of a 1 Ah cell, at 60 °C: a) after formation at 30% SoC; b) before cycling, at 30% SoC; c) after one cycle at C/20, between 3.0 and 4.35 V, at 0% SoC; after cycling, at 0% DoD.

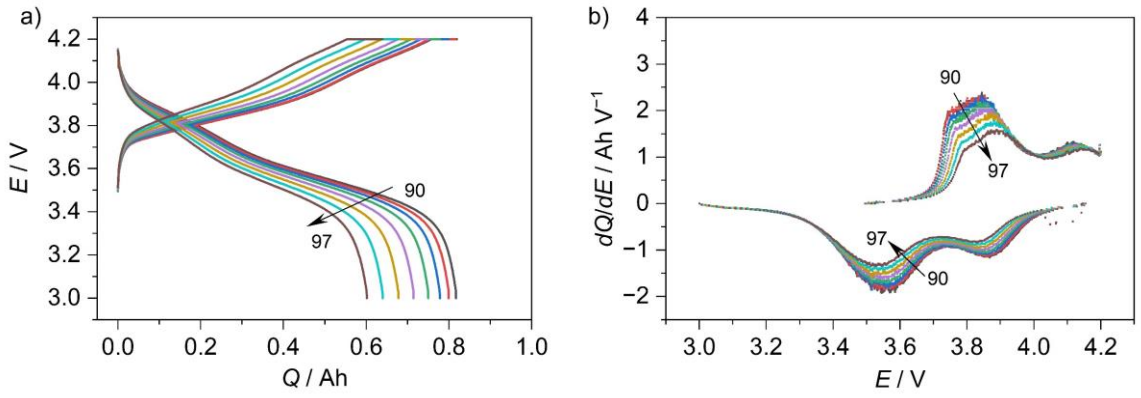

Figure S8. Electrochemical performance of a 1 Ah pouch cell cycled at C/10, 3.0 – 4.2 V, 60 °C, and an initial pressure of 3 kg·cm^{-2}. a) voltage profiles from cycle 90 to cycle 97; b) differential capacity profiles from cycle 90 to cycle 97.

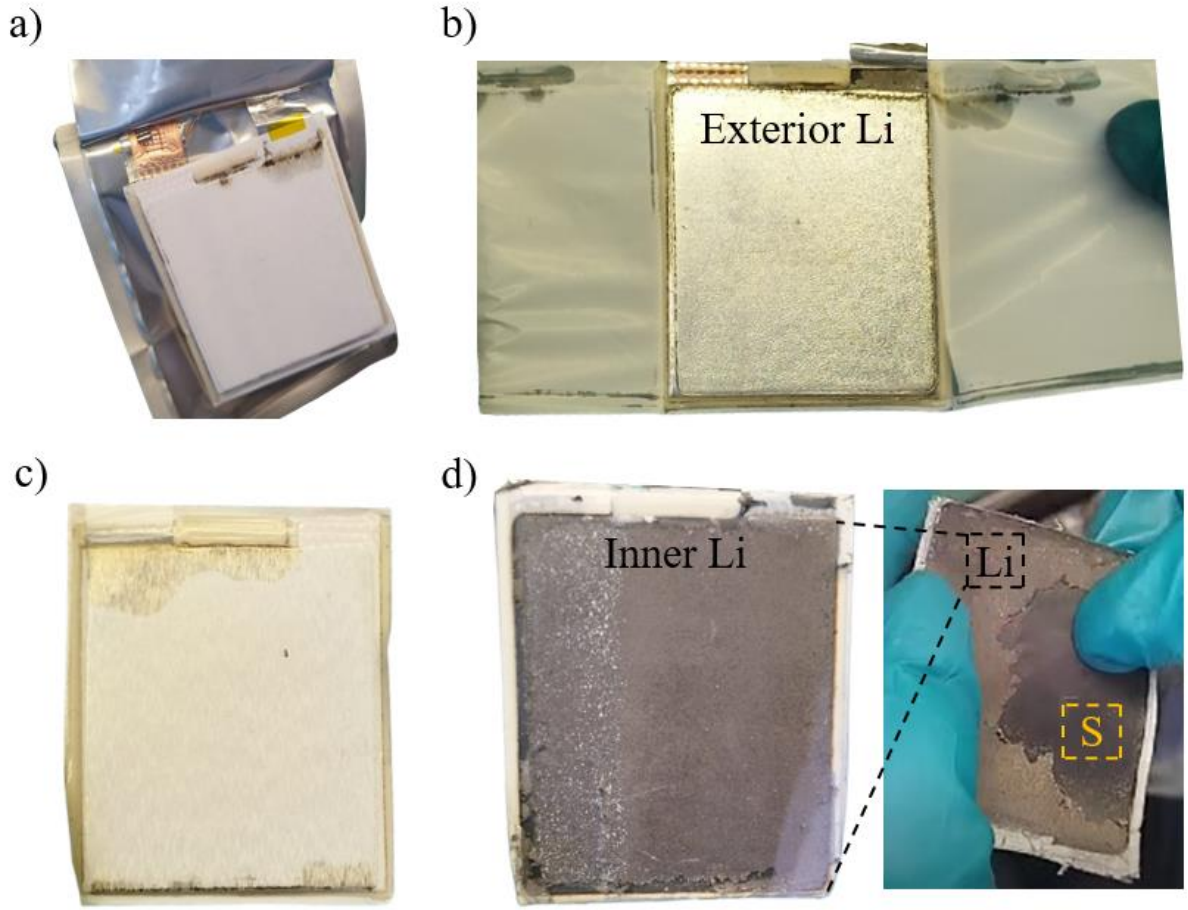

Figure S9. Individual cell components retrieved from an aged 1 Ah pouch cell. a) Exterior Celgard 2500 separator which was not in contact with other electrolyte components, b) Exterior Li electrode, c) Celgard 2500 separator which was in contact with Li electrode on one side [back side of (a)], d) A Li electrode retrieved from the center of the cell. The part marked as "S" shows the separator layer revealed after the Li was peeled off.

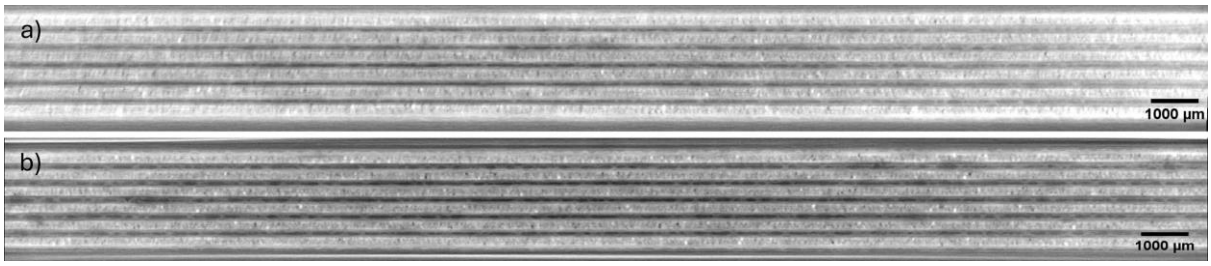

Figure S10. X-ray tomography images of two multilayer 1 Ah pouch cells after cycling at 60 °C, C/10.